Coplanar streams, pancakes and angular-momentum exchange in high-z disc galaxies — Source link ☒

Mark Danovich, Avishai Dekel, Oliver Hahn, Romain Teyssier

Institutions: The Racah Institute of Physics, Stanford University, University of Zurich

Topics: Disc and Disc galaxy

Related papers:

- Co-planar streams, pancakes, and angular-momentum exchange in high-z disc galaxies

- Cold streams in early massive hot haloes as the main mode of galaxy formation.

- How do galaxies get their gas

- Four phases of angular-momentum buildup in high-z galaxies: from cosmic-web streams through an extended ring to disc and bulge

- Galaxy bimodality due to cold flows and shock heating

Year: 2012

Coplanar streams, pancakes and angular-momentum exchange in high-z disc galaxies

Danovich, Mark ; Dekel, Avishai ; Hahn, Oliver ; Teyssier, Romain

Abstract: We study the feeding of massive galaxies at high redshift through streams from the cosmic web using the Mare Nostrum hydrocosmological simulation. Our statistical sample consists of 350 dark matter haloes of 1012 Msun at z= 2.5. We find that ˜70 per cent of the influx into the virial radius Rv is in narrow streams covering 10 per cent of the virial shell. On average 64 per cent of the stream influx is in one stream, and 95 per cent is in three dominant streams. The streams that feed a massive halo tend to lie in a plane that extends from half to a few Rv, hereafter 'the stream plane' (SP). The streams are typically embedded in a thin sheet of low-entropy gas, a Zel'dovich pancake, which carries ˜20 per cent of the influx into Rv. The filaments-in-a-plane configuration about the massive haloes at the nodes of the cosmic web differs from the large-scale structure of the web where the filaments mark the intersections of slanted sheets. The SP is only weakly aligned with the angular momentum (AM) near Rv, consistent with the fact that typically 80 per cent of the AM is carried by one dominant stream. The galactic disc plane shows a weak tendency to be perpendicular to the large-scale SP, consistent with tidal-torque theory. Most interesting, the direction of the disc AM is only weakly correlated with the AM direction at Rv. This indicates a significant AM exchange at the interphase between streams and disc in the greater environment of the disc inside an 'AM sphere' of radius ˜0.3Rv. The required large torques are expected based on the perturbed morphology and kinematics within this interaction sphere. This AM exchange may or may not require a major modification of the standard disc modelling based on AM conservation, depending on the extent to which the amplitude of the disc AM is affected, which is yet to be studied.

Co-planar streams, pancakes, and angular-momentum exchange in high-z disc galaxies

Mark Danovich[1] $\star$, Avishai Dekel[1]†, Oliver Hahn[2], Romain Teyssier[3,4]

[1]*Racah Institute of Physics, The Hebrew University, Jerusalem 91904, Israel*
[2]*Kavli Institute for Particle Astrophysics and Cosmology, SLAC/Stanford University, 2575 Sand Hill Road, Menlo Park, CA 94025, USA*
[3]*CEA, IRFU, SAp, 91191 Gif-sur-Yvette, France*
[4]*Institute for Theoretical Physics, University of Zurich, CH-8057 Zurich, Switzerland*

ABSTRACT

We study the feeding of massive galaxies at high redshift through streams from the cosmic web using the Mare Nostrum hydro-cosmological simulation. Our statistical sample consists of 350 dark-matter haloes of $\simeq 10^{12} M_\odot$ at $z = 2.5$. We find that $\sim 70\%$ of the influx into the virial radius R_v is in narrow streams covering 10% of the virial shell. On average 64% of the stream influx is in one stream, and 95% is in three dominant streams. The streams that feed a massive halo tend to lie in a plane that extends from half to a few R_v, hereafter "the stream plane" (SP). The streams are typically embedded in a thin sheet of low-entropy gas, a Zel'dovich pancake, which carries $\sim 20\%$ of the influx into R_v. The filaments-in-a-plane configuration about the massive haloes at the nodes of the cosmic web differs from the large-scale structure of the web where the filaments mark the intersections of slanted sheets. The stream plane is only weakly aligned with the angular momentum (AM) near R_v, consistent with the fact that typically 80% of the AM is carried by one dominant stream. The galactic disc plane shows a weak tendency to be perpendicular to the large-scale SP, consistent with tidal-torque theory. Most interesting, the direction of the disc AM is only weakly correlated with the AM direction at R_v. This indicates a significant AM exchange at the interphase between streams and disc in the greater environment of the disc inside an "AM sphere of radius $\sim 0.3 R_v$. The required large torques are expected based on the perturbed morphology and kinematics within this interaction sphere. This AM exchange may or may not require a major modification of the standard disc modeling based on AM conservation, depending on the extent to which the amplitude of the disc AM is affected, which is yet to be studied.

Key words: cosmology: theory — galaxies: evolution — galaxies: formation — galaxies: haloes — galaxies: kinematics and dynamics — galaxies: spiral — large-scale structure of Universe

1 INTRODUCTION

The
large-scale distribution of matter in the universe, dominated by the dark matter, exhibits a cosmic web (Bond et al. 1996; Pogosyan et al. 1998). This has been envisioned based on the Zel'dovich approximation (Zeldovich 1970) and the theory of Gaussian random fields (Doroshkevich 1970; Bardeen et al. 1986), reproduced in cosmological N-body simulations (Klypin & Shandarin 1983; Davis et al. 1985; Springel et al. 1996; Klypin et al. 2011), and observed in redshift surveys (Hucra et al. 1983; Colless 1999;

Adelman-McCarthy 2008). The honey-comb-like structure consists of big voids surrounded by flat low-overdensity sheets (walls, pancakes), that intersect in narrow, denser filaments, which further intersect in relatively compact, virialized, spheroidal dark-matter haloes (clusters) at the nodes of the web. According the quasi-linear Zel'dovich approximation (Zeldovich 1970), each Lagrangian point is characterized by the eigenvectors and eigenvalues of the deformation tensor, which consists of the second spatial partial derivatives of the gravitational potential field. if we denote the eigenvalues $(\lambda_1, \lambda_2, \lambda_3)$, ordered such that $\lambda_1 \geqslant \lambda_2 \geqslant \lambda_3$, a sheet would form due to a one-dimensional collapse where λ_1 dominates, which we can crudely approximate by the requirement that the signature of the eigenvalues is $(+, -, -)$. A filament would form after

$\star$ E-mail: mark.danovich@mail.huji.ac.il
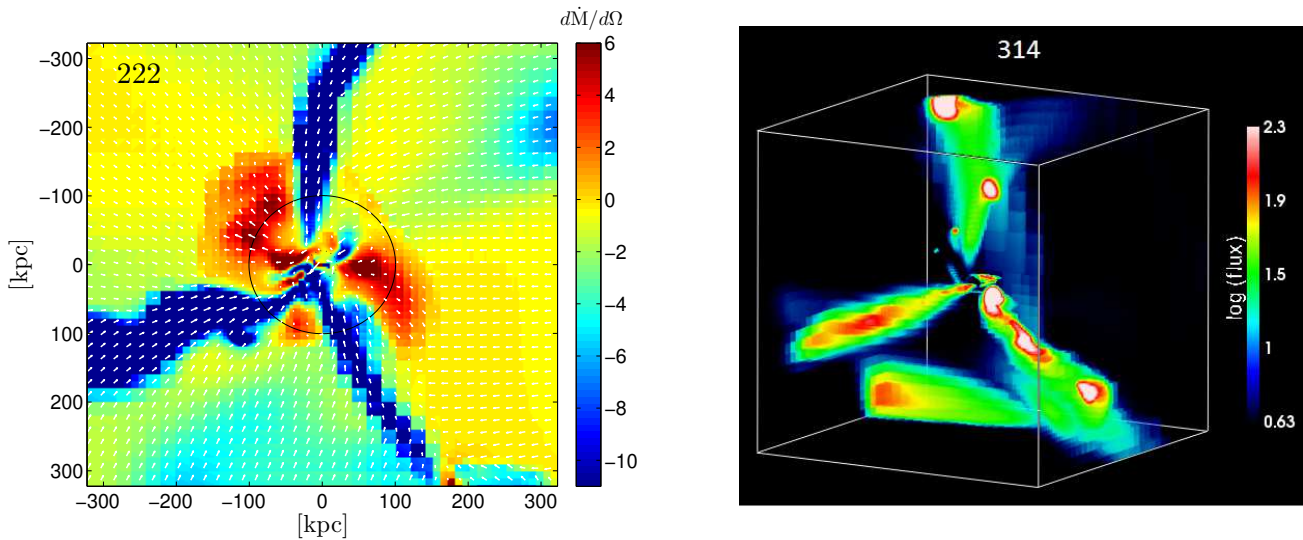† E-mail: avishai.dekel@huji.ac.il

Figure 1. Cold gas streams. Shown is the radial flux density per solid angle (in $M_\odot \, \mathrm{yr}^{-1} \, \mathrm{rad}^{-2}$) into two typical massive galaxies at $z = 2.5$ from the Mare Nostrum cosmological simulation. **Left:** A 1-kpc thick slice through the centre of a halo, showing three streams that emerge at a distance more than 5 times the virial radius (black circle) and penetrate to the inner halo. **Right:** a three-dimensional view of influx, extending to twice the virial radius, showing that the streams contain clumps and a smoother gas component. The clumps are merging galaxies containing gas, stars and dark matter, (see Dekel et al. 2009; Ceverino et al. 2010).
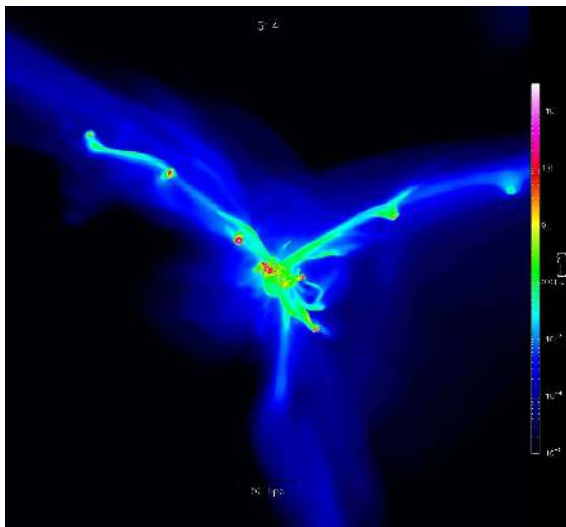

Figure 2. Gas density in the streams feeding the galaxy shown in the right panel of Fig. 1 (314), in a RAMSES test run with a resolution higher by an order of magnitude. The box encompasses a sphere of twice the virial radius. The stream configuration remains qualitatively similar, with the inner structure of the streams better resolved (courtesy of D. Tweed).

collapse in two directions, where λ_1 and λ_2 are comparable and much larger than λ_3, e.g., a signature $(+, +, -)$. A halo would form in a node, where the eigenvalues are all comparable and positive, $(+, +, +)$. The filaments thus form in the intersections of sheets, and the nodes are intersections of filaments. In the quasi-linear regime, the matter flows away from the voids into the sheets, within the sheets toward the filaments, and along the filaments toward the nodes.

The filaments are the prominent features of the cosmic web, both in terms of mass content and density contrast. In the linear regime of a Gaussian random density fluctuation

field, the fraction of volume and mass associated with each of the four different signatures of the deformation tensor is 42% for the filaments and sheets, and 8% for the haloes and voids (Doroshkevich 1970). In the non-linear regime, the statistics depend on scale, as the structures have collapsed bottom-up to increasingly higher densities occupying smaller and smaller scales. Hahn et al. (2007) have demonstrated this scale dependence by showing how the volume fractions of the four signatures of the deformation tensor deviate from the Gaussian random field values as the smoothing scale is decreased. Using adaptive filtering, Aragón-Calvo et al. (2010) found that the mass fractions associated with the four signatures of the Hessian tensor, consisting of the spatial partial derivatives of the density field, are 28.1% in haloes, 39.2% in filaments, 5.5% in sheets and 27.2% in voids, while these structures occupy 0.4%, 8.8%, 4.9% and 85.9% of the volume, respectively. The corresponding mean overdensities with respect to the mean cosmological background are 73, 4.5, 1.1 and 0.3, respectively. Using an excursion-set model for triaxial collapse, Shen et al. (2006) found that at $z = 0$, when filtering over scales corresponding to $10^{10} \, M_\odot$, typically 99% of the mass has crossed the threshold for collapse along at least one axis, and thus resides in sheets (including filaments and haloes), while 72% is in filaments (including haloes) of smaller scales embedded in these sheets, and only 46% is in haloes. Thus, no matter how we look at it, the filaments contain the largest fraction of mass, and their higher density contrast makes them much easier to detect than the sheets. Several other studies have addressed the large-scale geometry of cosmic-web filaments in simulations (e.g., Colberg et al. 2005; Hahn et al. 2007, 2009; Gay et al. 2010; Aragón-Calvo et al. 2010; Noh & Cohn 2011), and how to trace it in the observed distribution of galaxies (e.g., Dekel & West 1985; Aragón-Calvo et al. 2007; Sousbie 2011; Sousbie et al. 2011). Massive galaxies at redshift

$z \geqslant 2$ form in dark-matter haloes that are much more massive than the typical halo at that time, hundreds of times larger than the characteristic Press-Schechter mass (which is $\sim 3 \times 10^9 M_\odot$ at $z = 2.5$ for the WMAP7 cosmological parameters). They are therefore "high-sigma peaks" of the initial density fluctuation field, which reside in the nodes of the cosmic web. In each halo, the dark matter flowing along the filaments feeds the dark matter halo and fills the entire virial sphere. The baryons that stream with the dark matter along the filaments into the halo virial radius penetrate through the halo and feed the galaxy at the halo centre, both as merging galaxies and a smoother gas component (Birnboim & Dekel 2003; Keres et al. 2005; Dekel & Birnboim 2006; Ocvirk et al. 2008; Dekel et al. 2009). This is illustrated in Fig. 1, showing the influx density per solid angle on the scale of a few virial radii in two galaxies from the Mare Nostrum cosmological simulation (Ocvirk et al. 2008) used in Dekel et al. (2009) and in the current paper.

Figure 2 shows the gas density in the streams that feed the same galaxy shown in the right panel of Fig. 1, galaxy 314 of the Mare Nostrum simulation, which has been displayed in more detail in Dekel et al. (2009). The current map is from a test run using RAMSES with a maximum resolution of $60 \, \mathrm{pc}$, higher by more than an order of magnitude than the Mare Nostrum resolution. This figure demonstrates that the general stream pattern is not affected by the resolution, except that the inner structure of the streams and the smaller merging galaxies are better resolved.

The efficient feeding of galaxies by streams has a major impact on the way these galaxies form and evolve (Dekel & Birnboim 2006; Dekel et al. 2009; Ceverino et al. 2010; Oser et al. 2010; Ceverino et al. 2011; Cacciato et al. 2011). The streams bring in most of the baryonic mass and angular momentum, and are thus responsible for the formation of large rotating discs. The continuous intense in-streaming allows for high star formation rates (SFR) in those discs, in most cases not related to mergers (Genzel et al. 2006; Dekel et al. 2009). The streams maintain a high gas fraction that is responsible for a violent disc instability with large transient features and giant clumps, which drive a rapid mass inflow to the centre (independent of whether the clumps disrupt Dekel et al. 2009; Genel et al. 2012; Hopkins et al. 2012). This may eventually lead to the formation of a central bulge with a massive black hole (Dekel et al. 2009; Ceverino et al. 2010; Bournaud et al. 2011). A study of the baryonic stream properties is therefore crucial for a better understanding of galaxy formation at high redshift. In addition, since the gas tends to condense in the central, denser regions of the more dispersive dark-matter filaments and sheets, the gas can also serve as a unique tracer of the cosmic web skeleton in the vicinity of its high-sigma peak nodes.

In this paper we use a hydrodynamical cosmological simulation, the Mare Nostrum simulation, to study the large-scale properties of the streams feeding massive galaxies at high redshift. We also make a preliminary attempt at relating the angular momentum (AM) of disc galaxies to the AM carried by the streams from the cosmic web into the halo. The outline of the paper is as follows: In §2 (and §A) we describe the simulation and the method of analysis. In §3 we study the tendency of the streams to be co-planar and

the first detection of pancakes in cosmological simulations, to be studied in detail in Hahn et al. (2011). In §4 we investigate the distribution of influx in streams and pancakes, revealing one dominant stream and a tendency for three major streams. In §5 we address the angular momentum transport by streams from outside the halo into the inner disc, by exploring the degree of alignment between the stream plane and AM at the virial radius and between them and the disc. In §6 we discuss the possible origin of the main features of the cosmic web near a node. In §7 we summarize our results and discuss them. We address several technical issues in the appendices. Of particular interest is §C, where we evaluate a potential systematic effect in our analysis, namely the numerical tendency of alignment between the disc and the axes of the simulation grid.

2 METHOD

2.1 The cosmological simulation

The cosmological simulation used in this analysis is the AMR Horizon Mare Nostrum (MN) galaxy formation simulation (Ocvirk et al. 2008), which utilized the AMR code RAMSES (Teyssier 2002) to simulate the dynamics of gas and dark matter in a cosmological box. The standard ΛCDM cosmology is assumed, with $\Omega_\Lambda = 0.7$, $\Omega_\mathrm{m} = 0.3$, $\Omega_\mathrm{b} = 0.045$, $h = 0.7$ and $\sigma_8 = 0.95$ in a periodic box of side $50 \, h^{-1} \mathrm{Mpc}$. The dark-matter component is represented by 1024^3 particles of $1.17 \times 10^7 M_\odot$ each. A basic grid of 1024^3 cells is progressively adapted when the number of DM particles in the cell exceeds 8, or when the gas mass exceeds 8 times the initial gas mass resolution.. The minimum cell size is $1 \, \mathrm{kpc}$ physical. The large cosmological box and the 1-kpc resolution allows for a reliable statistical study of the way massive galaxies are fed from the cosmic web at the halo scales. This resolution allows for identifying massive discs that extend to $\sim 10 \, \mathrm{kpc}$, but the disc thickness is barely resolved. The MN simulation employs at the sub-grid level physical processes that are relevant for galaxy formation, such as star formation, supernovae feedback, metal enrichment, metal dependent cooling and background UV heating (see appendix §A). However, these processes are followed with a limited accuracy that is dictated by the limited resolution.

2.2 Dark Matter haloes and galaxies

We select from the MN snapshot at $z = 2.5$ all the 351 dark-matter haloes with virial mass in the range $(0.8 - 3) \times 10^{12} M_\odot$ (serially numbered 50 to 400 in order of decreasing mass). This is the mass range of haloes that host the massive star-forming galaxies observed at these redshifts (Genzel et al. 2006, 2008; Tacconi 2008; Dekel et al. 2009), with a comoving number density of $4 \times 10^{-4} \, \mathrm{Mpc}^{-3}$ for $M_\mathrm{v} > 1.5 \times 10^{12} M_\odot$ at $z = 2.5$. These haloes are expected to be relatively rare ($> 2\sigma$) density peaks at the nodes of the cosmic web, and are predicted to have shock-heated hot media penetrated by narrow cold streams (Dekel & Birnboim 2006; Dekel et al. 2009).

For each halo, we define the centre as the peak of the gas density smoothed with a Gaussian of standard deviation

5.4 kpc. We then use the gas density and velocity in 256^3 cells of a cubic grid about the galaxy centre. For a study on the halo scale at the highest resolution, the cell side is 1.246 kpc ($= 50/2^\ell \, h^{-1}\mathrm{Mpc}$ comoving at adaptive level $\ell = 14$) and the corresponding box side is 319 kpc, almost encompassing a $2R_\mathrm{v}$ sphere. For a study of the greater environment of the halo, we use boxes and cells twice and four times as large (adaptive levels $\ell = 13$ and 12), reaching to $\sim 5.5 R_\mathrm{v}$.

The gas velocities are corrected to the rest frame of the centre of mass of the cold gas with $T < 10^5\mathrm{K}$ within a sphere of radius $0.1 R_\mathrm{v} \sim 10\,\mathrm{kpc}$ about the density peak, mimicking the centre of mass of the disc. In most cases this correction is smaller than one resolution element and it has a negligible effect on the results. A Hubble flow ($H = 254\,\mathrm{km\,s^{-1}\,Mpc^{-1}}$ at $z = 2.5$) is added to the comoving velocities used in the simulation. Angular momentum is computed about the position of this centre of mass. Our results concerning inflows and angular momenta were tested not to be sensitive to the exact choice of disc centre and rest frame, which can be determined at an accuracy level that is comparable to the simulation resolution.

We exclude from the analysis 15 haloes where there is no obvious central galaxy in the halo, presumably due to ongoing major mergers. This leaves us with a sample of 336 haloes.

2.3   Identification of streams

The streams consist in principle of dark matter, stars and gas, but our previous attempts to quantify stream statistics based on the dark matter led to noisy results, that got worse at smaller radii inside the haloes where the dark matter is virialized. Here we identify the streams and study their properties based on the cold gas, which, due to dissipative processes, traces much more cleanly the filamentary skeleton of the cosmic web.

The main quantity used at every point $\vec{r}$ on a spherical grid about the galaxy centre is the radial flux density per solid angle,

$$\frac{d\dot{M}}{d\Omega} = \rho v_r r^2, \tag{1}$$

where ρ is the gas density, v_r the radial velocity and r the radial distance from the galaxy centre. We use in the analysis thin spherical shells of one-cell thickness or the average over several thin shells inside a thick shell. The scalars given in the cells of the cubic grid are interpolated into a spherical grid of 512^2 equal-area angular cells, with a radial thickness of $\sqrt{3} \times 50/2^\ell \, h^{-1}\mathrm{Mpc}$, where ℓ is the adaptive level used for the cubic grid that samples that shell (see §2.2).

In each shell, we identify streams by first applying a given influx density threshold, at a given overdensity above the average influx density in the entire shell. We then apply an angular friends-of-friends algorithm to the influx above the threshold on the spherical shell grid. This means that we assign to the same stream all the adjacent grid cells with influx density above the threshold (see §4 for more details). For each stream, we record its flux-weighted average angular position on the sphere and its total mass inflow rate.

In our analysis of the streams flowing into the virial radius, we sometimes consider the sum of all the spherical shells in the radius range $(1 - 2)R_\mathrm{v}$. This stacking improves the statistics by including more information, and in particular it emphasizes elongated radial streams that stretch over a virial-radius scale. It properly smoothes over the local fluctuations due to merging galaxies, putting them in the context of the streams that they belong to.

2.4   Numerical Alignment

A potential caveat in our analysis of preferred planes is the numerical tendency for artificial alignment of planes of matter with the simulation grid. A grid-based Poisson solver, and in particular the hydrodynamical solver, create non-physical forces along the preferred Cartesian directions of the simulation grid, which act to align the mass distribution with the grid (Hahn et al. 2010). This is especially relevant for the galactic disc plane, which involves scales not much larger than the resolution scale, but it would also be useful to verify that no artificial alignment propagates to the sheets on larger scales (to be defined below). The artificial alignment is expected to be stronger at lower redshifts, where the discs might have had enough time to relax to the closest grid direction, so we expect our analysis of massive galaxies at $z = 2.5$ to be less vulnerable to this numerical effect, despite the 1-kpc resolution.

We address this potential numerical alignment in appendix §C. We find that it is limited to $\sim 20\%$ of the discs. For cases where the original cosine of the angle between the normal to the disc and the closest grid axis was $\cos\theta > 0.8$, it has been pushed up by $\Delta(\cos\theta) \sim 0.08$. This is a rather small effect, associated with a negligible shift in the mean of $\cos\theta$. This is the level of error that we should assign to any measure of alignment between the disc and other planes. As expected, the stream plane at R_v does not show any measurable numerical alignment with the simulation grid.

3   STREAM CO-PLANARITY

In the large-scale cosmic web, where the filaments bridge between the nodes to form a three-dimensional network, there is no obvious a priori reason for the filaments that feed a node to lie in one plane. We find below that they do tend to lie in a plane that contains the galaxy centre, which we term "the stream plane" (SP). Figure 3 shows the influx in a thick shell at $(1 - 2)R_\mathrm{v}$ for twelve different simulated galaxies. The haloes shown were selected from the large sample of haloes that have at least three streams (according to our definition of stream number described below) and they are very well confined to a great plane (namely a plane that contains the galaxy centre). The coordinates are rotated such that the best-fit stream plane is at the equator. We find using the goodness of fit measure (described below) that 60% of the galaxies fit a plane better than the worst case shown in the figure (halo 145). Examples of galaxies in which the fit to a plane is worse are shown in appendix §D.

3.1   The best-fit Stream Plane

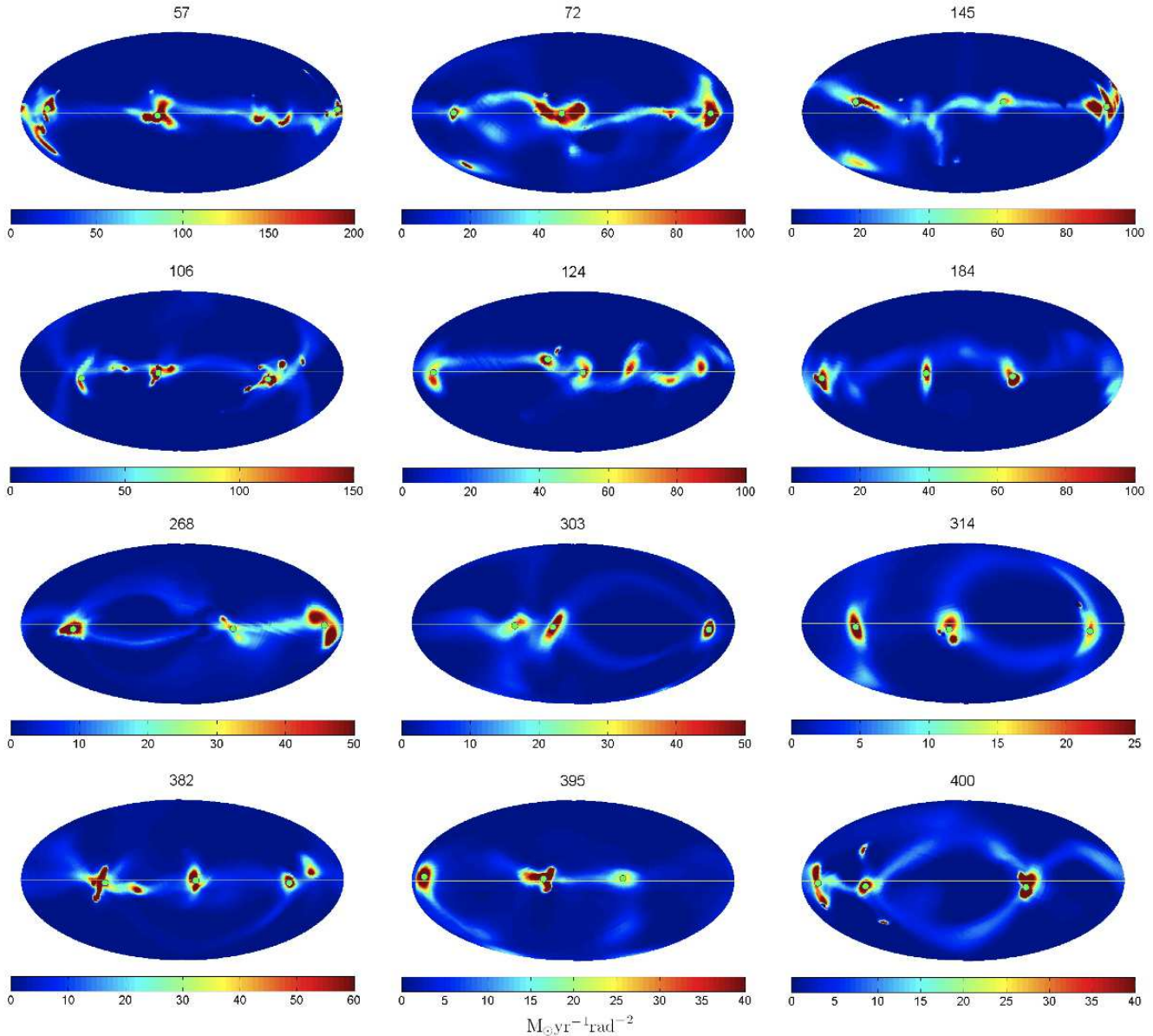We define the best-fit stream plane and measure the quality of the fit based on the angular positions of the centres

Figure 3. Co-planar inflowing streams and pancakes in a thick shell at $(1-2)R_{\rm v}$. Shown as whole-sky Hammer-Aitoff maps of influx density are twelve different simulated galaxies in haloes of $\sim 10^{12}{\rm M_\odot}$ at $z = 2.5$. They are selected to represent the many galaxies with at least 3 streams that almost perfectly lie on a great plane. The coordinates are rotated such that the best-fit stream plane coincides with the equator. The color represents radial influx of gas mass per solid angle. The centres of the three streams with the highest influx are marked by green dots. Typical flux densities in the streams are $(50-150)\, M_\odot\, {\rm yr}^{-1}\, {\rm rad}^{-2}$ with the higher fluxes valid in the more massive haloes. Thin pancakes of $\sim 10-15\, M_\odot\, {\rm yr}^{-1}\, {\rm rad}^{-2}$ are seen between the streams, most frequently coinciding with the stream plane, but sometimes showing pancake segments that deviate from the stream plane.

of the three streams with the largest influx at $(1-2)R_{\rm v}$. One or two streams always lie on a plane that contains the galaxy centre, so three is the smallest number of streams for which co-planarity is nontrivial. We thus eliminate from the analysis of co-planarity the haloes with less than three streams (see below). We will show that typically more than 90% of the influx in streams is carried by the three leading streams, so using these three for the fit and ignoring any additional streams is quite sensible. We limit the fit to a fixed number of streams (3) in order to properly compare to a null hypothesis of random angular positions without worrying about the dependence of the co-planarity on the number of

points. For a similar reason, when we fit a plane we do not weigh the three streams by their individual influxes.

The three streams for the fit of a plane are determined after applying the two following procedures. First, if two streams are separated by less than a minimum angular separation $s_{\rm min}$, we combine them into one, with the sum of the mass inflow rates and a new inflow-weighted centre. This is in order to avoid confusion with two apparently nearby streams that may actually be part of one stream and may lead to a trivial co-planarity. Second, and what turns out to make a stronger effect, we eliminate from the analysis haloes in which the ratio of inflow rate in the third stream
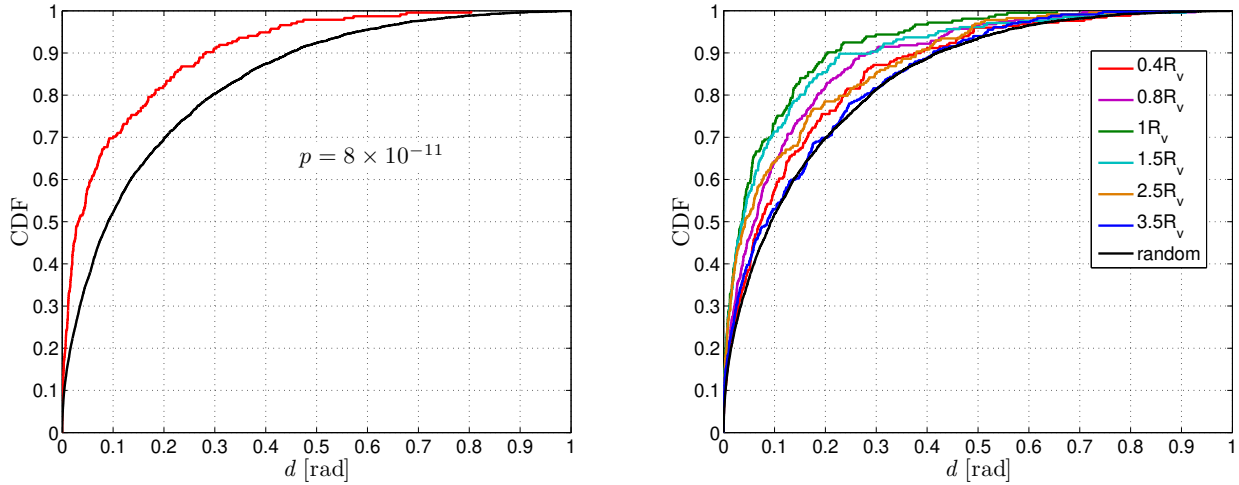
Figure 4. The significance of the stream co-planarity in a shell $(1-2)R_{\mathrm{v}}$ (left) and in shells of different radii (right). Shown is the cumulative probability distribution (CDF) of the rms deviation of the three largest streams from the best-fit plane, d, based on 235 haloes (color). It is compared to the same CDF for the null hypothesis of a random angular distribution of 3 points, based on 5,000 realizations (black). The same threshold s_{min} is applied to the data and the null model. A KS test reveals that at R_{v} the null hypothesis is strongly rejected with a p value of 8×10^{-11}. The corresponding p-values for shells from $0.4R_{\mathrm{v}}$ to $3.5R_{\mathrm{v}}$ are: $0.12, 7 \times 10^{-5}, 2 \times 10^{-12}, 2 \times 10^{-8}, 4 \times 10^{-6}, 0.38$.

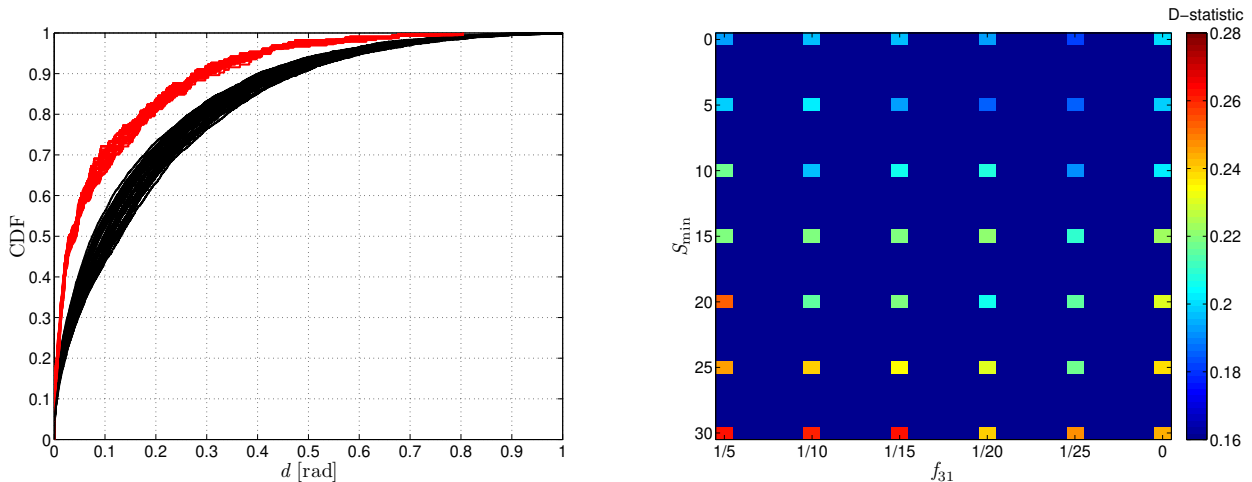**Figure 5.** Sensitivity to the procedure of identifying the streams. **Left:** Shown are the CDFs of d for different values of s_{min} and f_{31}, for the simulated haloes (red) and the random-position null model (blue). **Right:** The D statistic of the KS-test (in color) for different combinations of s_{min} and f_{31}. The results are insensitive to the choice of parameters in the given range.

compared to the first stream is smaller than a threshold f_{31}. If this ratio is below the threshold, we consider the halo to be of two streams or less, where the fit to a plane should be trivial, and eliminate it from the analysis of co-planarity. These procedures reduce the number of haloes that we use in our statistical analysis concerning the stream plane from 336 to 235. The main selection is due to the threshold f_{31}, which with $f_{31} = 0.1$ filters out 92 of the 101 haloes that are eliminated from the co-planarity analysis.

The deviation of the three streams at a given concentric shell from a given great plane is defined by the sum in quadrature of the angular distances between the stream centre angular positions and the great circle of intersection between the plane and the shell. The best-fit plane is determined by minimizing this sum, and the minimum value,

d in radians, is used as a measure of the deviation from a plane.

In appendix §B, we describe a different algorithm for defining the stream plane, which maximizes the inflow rate through a belt of width $\pm\pi/9$ radians about a great circle on the spherical shell. We find that in the vast majority of the haloes, at R_{v}, the stream planes defined by the two methods practically coincide, with a median of $\cos\theta = 0.96$ for the angle between the planes as defined by the two methods (Fig. 20).

3.2 The significance of the co-planarity

The statistical significance of the stream co-planarity is evaluated by comparing the data from the simulations to a
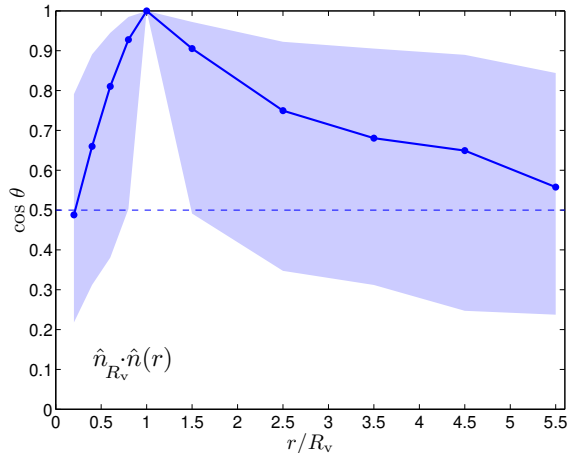
Figure 6. Extension of the streams plane. Shown is the median of the cosine of the angle between the SP at $1R_v$ and the SP at different radii from $0.2R_v$ to $5.5R_v$ compared to a random distribution in which the median is 0.5. It shows a significant alignment from $0.5R_v$ to $2.5R_v$ and a weak alignment for shells inside $0.5R_v$ and in the range $2.5 - 5.5R_v$.

null hypothesis where the streams represent three random points on the sky, obeying the same selection criteria based on s_{min} and f_{31}. We use a Kolmogorov-Smirnov (KS) test to compare the cumulative distribution functions (CDF) of the deviation from a plane, d, in the sample of simulated haloes compared to the null hypothesis. The KS-test allows to determine the statistical likelihood (p-value) that the two data sets are drawn form the same distribution. For the purpose of identifying the centers of the streams, the fiducial values for the selection parameters are chosen to be an influx density threshold for the stream identification of 5 times the mean influx density in the shell, and then $s_{min} = 15°$ and $f_{31} = 0.1$. The choice of an overdensity threshold of 5 helps sharpening the definition of the stream centers, but the results for thresholds of 3 and even 2 do not make a significant difference to the resultant co-planarity. Figure 4 (left) shows the two CDFs, revealing a significant difference between the simulated data and the random null model. With a sample of 235 simulated haloes, the maximum vertical separation between the CDFs is $D = 0.234$, implying that the null hypothesis is strongly rejected with a p value of 8×10^{-11}.

Figure 5 (left) shows the same CDFs for different values of s_{min} in the range $0 - 30°$ and f_{31} in the range $0 - 0.2$. The value of D for each combination of values for these parameters is also shown in Fig. 5 (right). The small variations in the KS-test results demonstrate that the significance of the stream co-planarity is not sensitive to the exact choice of values for the parameters used to select the streams for the fit.

3.3 Spatial extent of the streams plane

In order to address the spatial extent of the stream plane both outside the virial radius and inside the halo, we first inspect the alignment between the SP at R_v and the SP at other radii r in the range $0.2R_v$ to $5.5R_v$. The SP is identified using the same selection criteria at all radii. Figure 6 shows the median

and the 68% percentiles for the cosine of the angle between these planes as a function of r, compared to a random distribution where the median is 0.5. The average cosine is above 0.75 in the range $0.5 - 2.5R_v$, indicating a significant alignment of the SP in this range. Note that R_v itself is not a special physical radius, as the virial shock and the dark-matter virialization radius could actually be anywhere in this range. The figure would therefore be qualitatively similar had we anchored the curve at some other radius slightly different from R_v.

Outside the virial radius, the SP extends to beyond $5R_v$. KS-tests yield p values that range from 3×10^{-49} at $r = 1.5R_v$, through 5×10^{-11} at $r = 3.5R_v$, to 6×10^{-4} at $r = 5.5R_v$. This plane connects the neighborhood of the halo to the global cosmic web.

Inside the halo, the SP penetrates to $\sim 0.4R_v$, with the KS p values ranging from 10^{-53} at $r = 0.8R_v$ to 4×10^{-7} at $r = 0.4R_v$. However, at $r = 0.2R_v$, the SP no longer correlates with the SP at R_v, with a KS $p = 0.92$. This argues that the stream plane practically disappears at $r = 0.2R_v$ and inside it, the $20\,\mathrm{kpc}$ vicinity of the disc. We will get back to this in the discussion of angular momentum in §5.

A complementary way to examine the extension of the SP is by evaluating the goodness of fit to a plane in each radius. We apply a KS test similar to §3.2 to the streams at radii from $0.4R_v$ to $3.5R_v$. Figure 4 (right) shows the CDFs for the different radii, and the caption quotes the corresponding KS p values. We see that the co-planarity is highly significant for radii from $0.8R_v$ to $2.5R_v$, and it becomes much less significant both at $r \leqslant 0.4R_v$ and at $r \geqslant 3.5R_v$.

We note that the apparent disappearance of the stream plane in the inner halo may partly be attributed to the method of identification of streams, which becomes less reliable at small radii, where the streams occupy a larger angular area and the velocity field becomes much more complex (see §5.6 and Fig. 18 below).

3.4 Pancakes

While the qualitative tendency of the streams to be co-planar has been noticed already in Dekel et al. (2009), the Hammer-Aitoff projections at and outside R_v, like the ones shown for a sample of galaxies in Fig. 3, also reveal thin sheets of inflowing gas, typically filling the same plane defined by the streams, and sometimes hinting to additional planes or plane segments. This is a low-entropy gas, inflowing toward the central galaxy with a typical influx density $\sim 10\,M_\odot\,\mathrm{yr}^{-1}\,\mathrm{rad}^{-2}$, as opposed to $\sim 100\,M_\odot\,\mathrm{yr}^{-1}\,\mathrm{rad}^{-2}$ in the streams. Figure 7 highlights these sheets in three-dimensional images of gas influx density and gas density in three different haloes. In each case, the intense streams are embedded in a well-defined sheet of gas with influx density just above the threshold, extending to $5R_v$ and beyond. These are the pancakes envisioned by Zel'dovich (Zeldovich 1970), showing up for the first time so clearly in the gas distribution of cosmological simulations, as they are low-density features that are normally overwhelmed by the denser, more massive filaments.

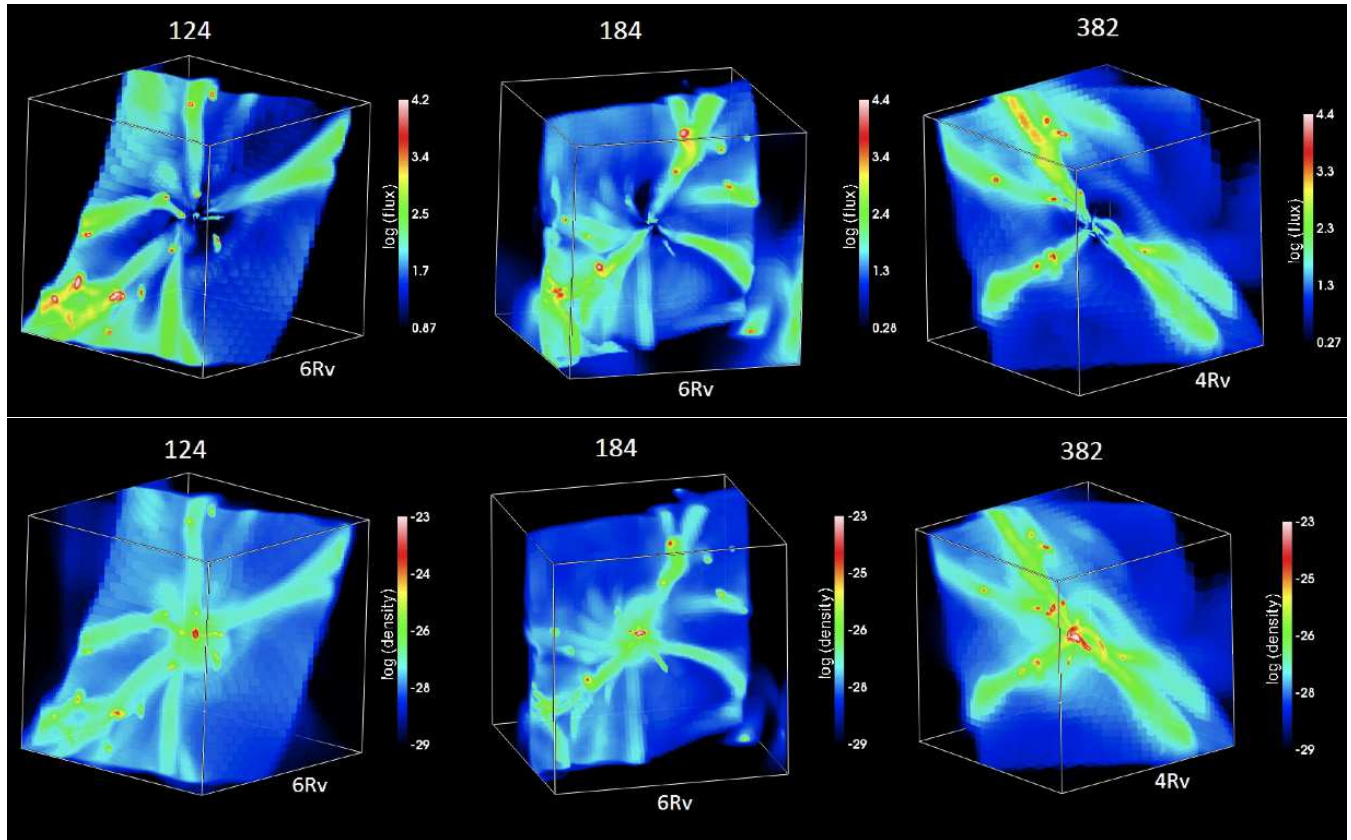Figure 8 shows three examples of haloes in which

Figure 7. Cold streams embedded in pancakes, flowing into three different simulated galaxies. The box side is marked in each case. No temperature threshold is applied. **Top:** log influx density (in $M_\odot \, \mathrm{yr}^{-1} \, \mathrm{rad}^{-2}$). **Bottom:** log gas density (in $\mathrm{g \, cm}^{-3}$). The planar pancakes and elongated streams become apparent in this ray-casting maximum-intensity projection, which shows the maximum intensity volumetric pixel along the line of sight.
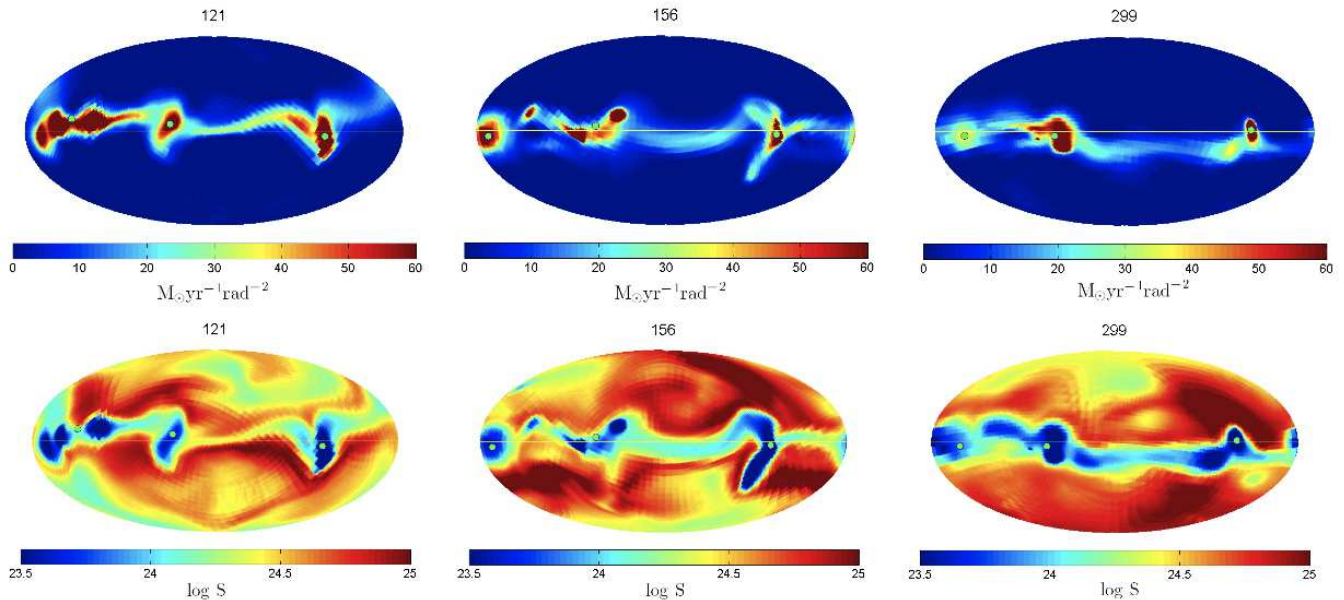

Figure 8. Pancakes at R_{v}. Shown are maps of influx density (top) and log entropy $S = T\rho^{-2/3}$ (bottom) in three simulated galaxies with dominant pancakes. No temperature threshold is applied. The coordinates are rotated such that the maximum influx is about the equatorial plane (appendix §B). More than 90% of the influx is in the $\pm\pi/9$ equatorial belt. The pancake and streams are of low entropy, bounded by high-entropy regions indicative of the planar shocks that resulted from the inflow of gas from the voids into the pancakes.
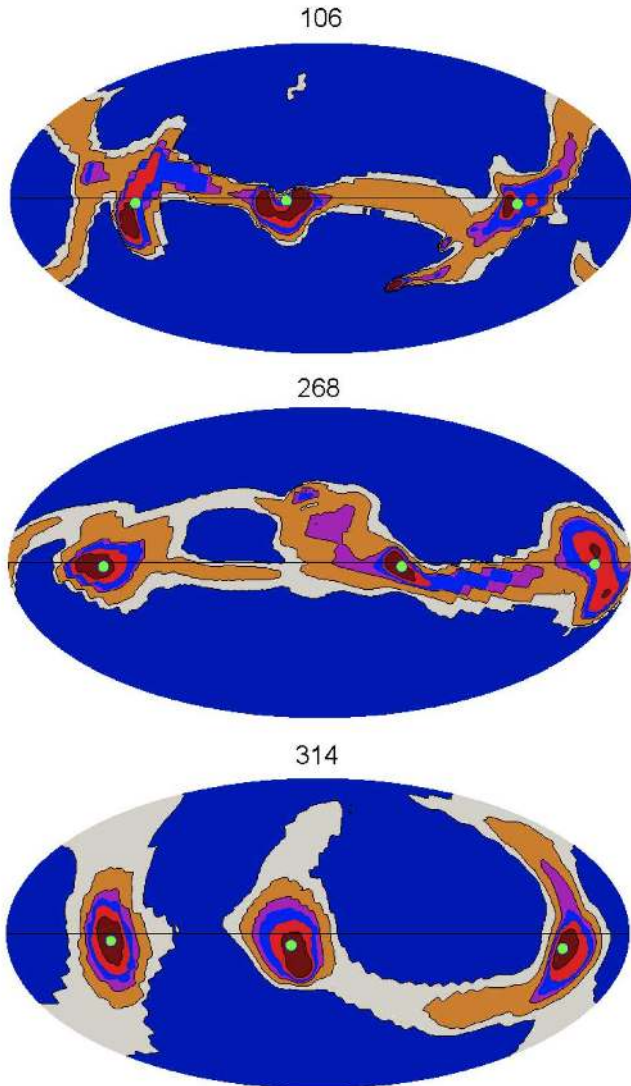
106

268

314

Figure 9. Influx density in streams and pancakes. Shown is influx density in Hammer-Aitoff maps of three haloes at $R_{\rm v}$. The contours refer to iso-influx-overdensity with respect to the mean influx density in the shell, at levels of 0.5 (grey), 1 (orange), 2 (purple), 3 (blue), 5 (red), and 8 (dark red). The pancakes are confined to influx overdensities in the range from below 1 to about 2. The streams are defined by influx overdensities of 2 (purple) and above. The mean values for the three examples are: $9.8, 5.8, 2.9\, M_{\odot}\,{\rm yr}^{-1}\,{\rm rad}^{-2}$. See Fig. 10 and Fig. 11.

the high influx density is largely confined to one obvious pancake and its embedded streams. In these cases the belt of $\pm\pi/9$ about the best-fit plane (§B), encompassing a third of the shell area, contains more than 90% of the total influx at $R_{\rm v}$. The entropy maps, where log entropy is measured from the gas temperature and density as $S = T\rho^{-2/3}$, demonstrate that the pancakes are regions of low entropy, hosting the denser, cold streams. The pancakes are bounded from above and below by regions of higher entropy, indicative of planar shocks that resulted form the gas flowing from the voids into the pancakes. The gas pancakes between the streams are explored in more detail in a companion paper using cosmological simulations of higher resolution (Hahn et al. 2011).

4 INFLUX IN 3 STREAMS AND PANCAKES

We now address the distribution of influx among the streams and in the pancakes. We explore the effective number of dominant streams, and justify our focus on the three dominant streams in the analysis of the stream plane in the previous section.

Figure 9 shows Hammer-Aitoff maps of influx overdensity with respect to the mean for each of three galaxies (§2.3), with an emphasis on the influx density levels associated with the streams and the pancakes. One can see that the streams are typically separated out for thresholds of ~ 2 times the mean influx density. Higher levels of influx overdensity define the central regions of the streams. We therefore use an overdensity threshold of 3 or 5 to define the stream centres. The pancakes are typically confined to influx overdensities in the range 0.5 to 2. The small angular area contained within an influx overdensity of order unity demonstrates the highly anisotropic pattern of cold gas streaming (see also Aubert et al. 2004).

Once the streams are identified for a given influx overdensity threshold, they are rank ordered by influx, from high to low. Figure 10 (left) shows the influx in the first N streams relative to the total influx in the shell at $R_{\rm v}$, for different values of the influx overdensity threshold, averaged over all 336 haloes. As described in §3.2, nearby streams have been merged based on $s_{min} = 15°$, and streams with influx much below the influx of the first stream were eliminated based on $f_{31} = 0.1$, but here the analysis was not restricted to haloes of three streams. With the lowest influx overdensity threshold, 0.5 of the mean, the influx is effectively in a single meta-stream, or a pancake, that carries more than 90% of the total influx in that shell. With an influx overdensity of 2 times the mean, for which the streams are already well separated, the first stream carries on average 49% of the total flux, the first three streams carry 68%, and all the streams carry 70%. The threshold overdensity of 2 is useful for capturing most of the influx in the streams while avoiding most of the off stream influx in the pancakes. In $\sim$ 90% of the haloes the dominant stream is the densest stream, and in 67% of the haloes the dominant stream has the highest inflow velocity. In most cases the densest stream is also the one with the highest velocity, but in 30% of the haloes the densest stream does not have the highest inflow velocity. Once the streams are separated, namely for thresholds of 2 and above, the shape of the curves seem to be rather independent of threshold, indicating that the distribution of flux in the streams relative to each other is robust, while the total influx in streams is obviously a decreasing function of the threshold level.

Figure 11 (left) shows the fraction of the shell area covered by the first N streams. For an influx overdensity of 2, the covering fraction by streams is about 10%. The area covered by the denser parts of the streams that carry more than half the total influx, defined by an influx overdensity of 4, is on average 5%. This is comparable to the area coverage estimated for Lyman-alpha absorption by cold streams from a central source, using simulations of higher resolution (Fumagalli et al. 2011; Goerdt et al. 2011).

Figure 11 (right) shows the fractional angular area covered by streams and pancakes as a function of the fraction of influx carried by these streams and pancakes, at $R_{\rm v}$.
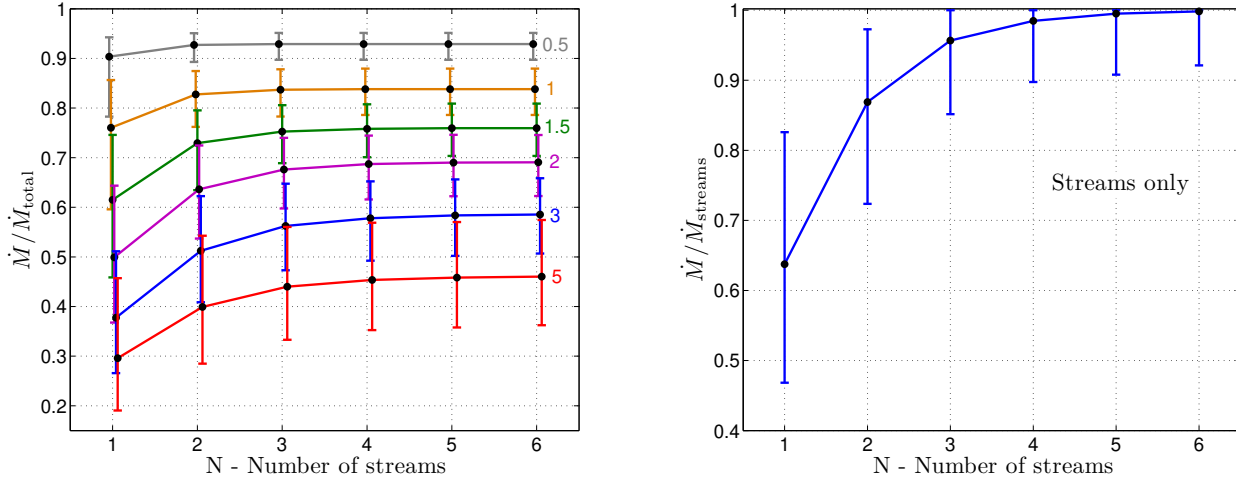
Figure 10. Fractional contribution of the first N streams to the total influx at $R_{\rm v}$ (left) and to the total influx in streams (right). Shown are the averages and standard deviations over the sample of 336 simulated haloes. The left panel compares different thresholds of influx overdensity. For example, with a threshold at an influx overdensity of 2, the first 3 streams carry on average 68% of the total influx. In the right panel the streams are defined by an influx overdensity of 3. The first stream carries on average 64% of the influx in streams, and the first three streams carry 95%.
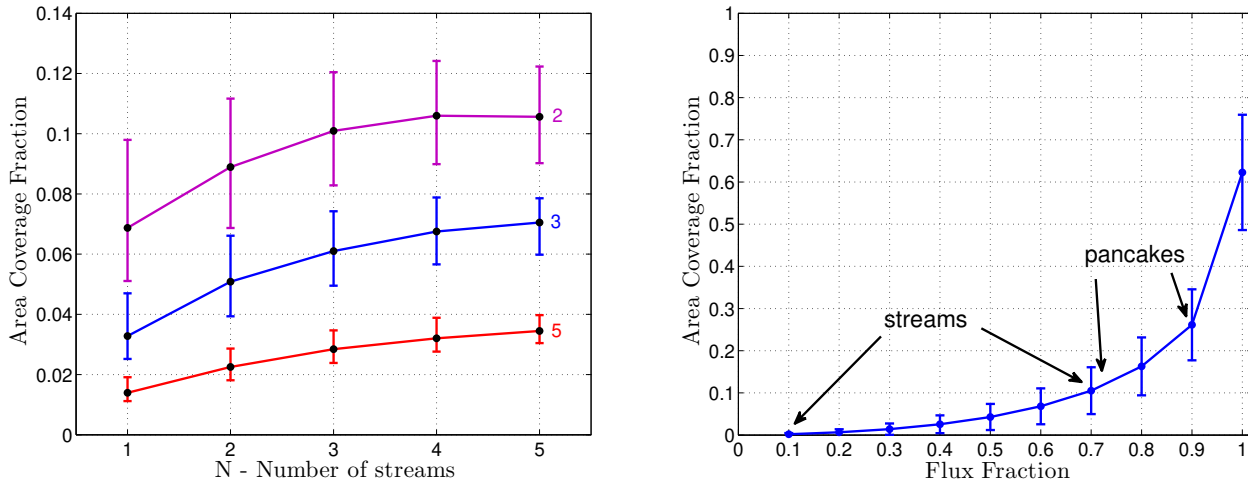

Figure 11. Fractional area coverage by streams and pancakes at $R_{\rm v}$ averaged over the 336 haloes. **Left:** area covered by the first N streams for flux overdensity thresholds 2,3,5. With a threshold overdensity of 2, the first 3 streams have an averaging covering fraction of 10%. **Right:** area coverage as a function of the corresponding fractional influx. The threshold of influx overdensity is varying along the curve, from $\gg 1$ to 2 for streams, and from 2 to 0.5 for pancakes. The streams carry on average about 70% of the influx and cover 10% of the angular area. The pancakes bring in about 20% of the influx in 20% of the area.
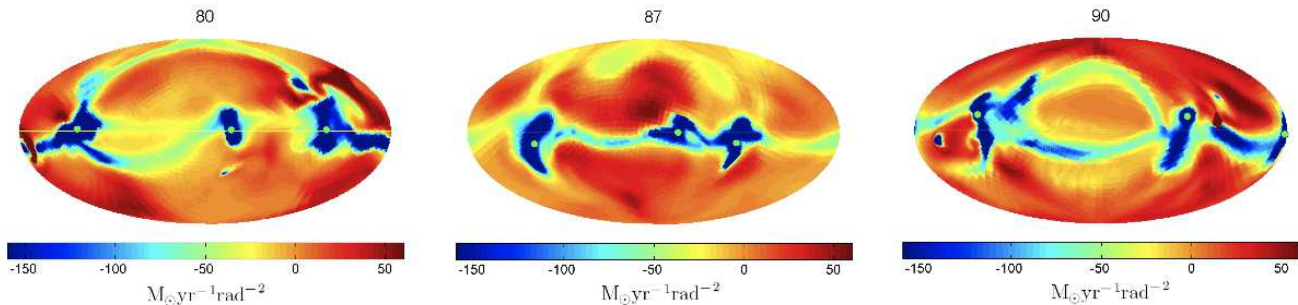

Figure 12. Outflowing versus inflowing gas at $R_{\rm v}$. Shown are Hammer-Aitoff projections of the flux density per solid angle for three haloes, outflowing (red) and inflowing (yellow to blue) gas. While the inflow is confined to narrow streams and thin pancakes, the outflows cover $\sim 50\%$ of the shell.
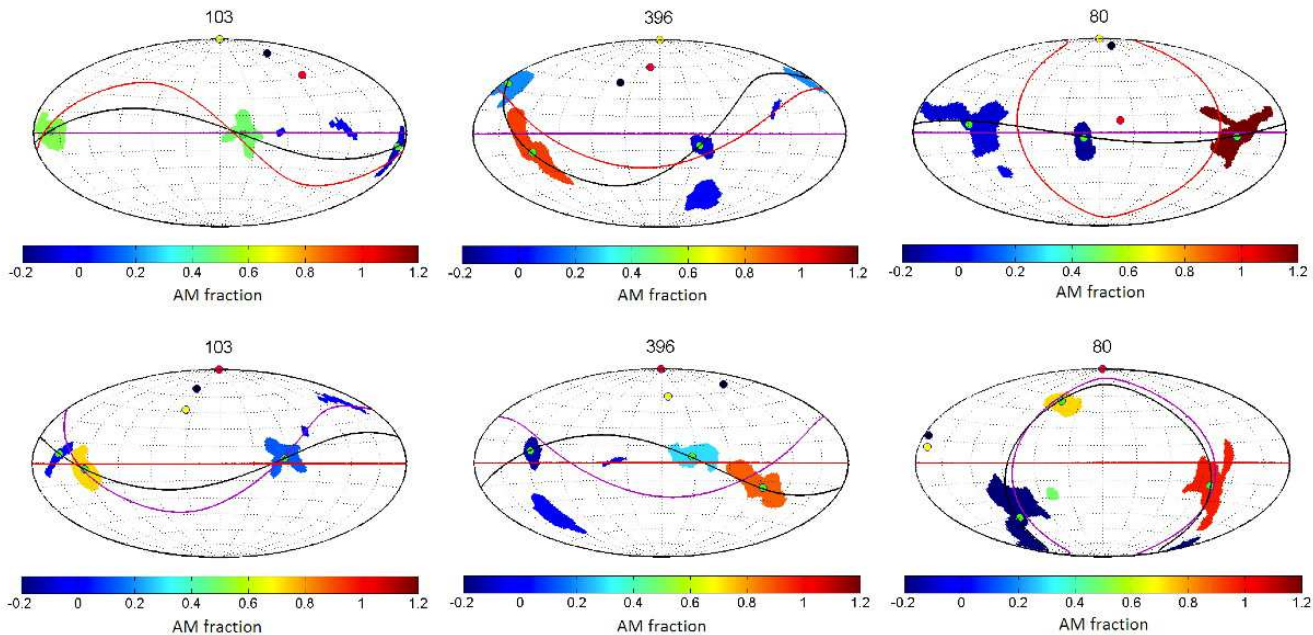
Figure 13. AM fraction in the streams at R_v shown in a Hammer-Aitoff projection. The three columns display three galaxies. Only cells with $V_r < -0.5V_v$ are included. Marked by a line and a small circle of the same color are three planes and the normals to them: The AM at R_v (purple), the stream plane (black), and the disc AM (red). **Top:** Fraction relative to the total AM at R_v, and rotated such that the AM plane at R_v is at the equator. **Bottom:** Referring to the AM component along the direction of the disc AM, and rotated such that the disc plane is at the equator. Between the two opposite orientations of the normal to the stream plane we show the one closest to the AM vectors.

The curve is constructed by varying the influx overdensity threshold (which is not explicit in the plot). The mean and standard deviation of the area coverage factor at a given flux fraction, over the 336 haloes, are shown. We see that on average 70% of the influx, at the highest influx overdensities, is limited to about 10% of the angular area — this is the influx in streams, as defined with a flux density threshold of 1.5-2. At lower influx overdensities, the following 20% of the influx is covering about 18% of the area, and can be associated with the pancakes. The final 10% of the influx is spread over about 30% of the area, mostly representing low-velocity infall not directly associated with the streams, that is unlikely to ever reach the inner disc.

The gas in 38% of the area is outflowing. Figure 12 shows via typical examples how the outflows find their way trough the broad dilute areas between the inflowing narrow streams and thin pancakes.

Figure 10 (right) shows the influx in the first N streams relative to the total influx in streams, averaged over the R_v shell for an influx overdensity threshold of 3 times the mean. We first note that the first stream is dominant — it typically carries 50-80% of the flux in streams. Then we see that on average 95% of the stream flux is carried by the first 3 streams (typically ranging from 85% to 100%). We learn that in the typical halo, for practical purposes, the influx is carried by *three dominant streams* with more than half the influx in *one dominant stream*. These estimates are robust — as seen in Fig. 10, they are not too sensitive to the influx overdensity threshold chosen in the identification of the streams.

Earlier related estimates of the effective number of streams can be found in Colberg et al. (2005), Pichon et al.

(2010), Aragón-Calvo et al. (2010) and Noh & Cohn (2011). Colberg et al. (2005) studied the dark matter filaments connecting pairs of haloes more massive than $10^{14} M_\odot$ on scales of $\sim 20 h^{-1} \text{Mpc}$. They find between one to four filaments per halo, consistent with our findings. They also find a marginal tendency for an increase in the number of filaments for more massive haloes. Aragón-Calvo et al. (2010) obtained similar results for the connectivity of clusters more massive than $10^{14} M_\odot$ with an average number of filaments in the range 2-5 depending on the mass of the cluster.

Being fed by co-planar streams, and having three major streams, of which one is dominant, are not obvious properties of nodes in a three-dimensional network. We discuss in section §6 tentative ideas concerning the origin of these features, but it largely remains an open theoretical question.

5 STREAM PLANE VS. DISC: ANGULAR MOMENTUM

The cosmic-web streams provide the gas for the buildup of a disc galaxy at the centre of the dark halo. The study of the stream properties provides vital information concerning the process of disc buildup, and especially the growth of the angular momentum (AM) that governs the disc size and structure. The unique geometrical structure of the in-streaming may help us visualize and better understand the AM evolution, which is otherwise quantified in a more abstract way by the tidal-torque theory (White 1984). The basic idea is that a small transverse velocity of the inflowing stream at a large distance results in a non-negligible impact

parameter relative to the disc centre, which is associated with a large AM that is being transported with the stream into the galaxy (e.g., Pichon et al. 2011).

Here we provide a preliminary study that focuses on the relative orientations of different relevant characteristic planes, as defined by the inflowing and accumulated gas component. On the halo scale, near $R_{\rm v}$, we compare the normal to the stream plane (which in many cases is closely related to the pancake plane) to the direction of the AM in a shell about $R_{\rm v}$. Both are then compared to the direction of the AM of the disc, defined as the AM of the gas in a sphere of radius $0.1R_{\rm v}$,[1] and then to the AM in shells at different radii inside and outside the halo. In this paper, the study is limited to the gas component, and to the $z = 2.5$ snapshot, thus not considering the time delay between the stream crossing of the virial radius and its arrival at the disc. Recall that the AM is computed about an origin that approximates the centre of mass of the disc, as described in §2.2.

5.1   Visual comparison of planes

In Fig. 13 we display for three haloes Hammer-Aitoff maps of the AM at $R_{\rm v}$ and compare the orientations of the three relevant planes: the stream plane and AM at $R_{\rm v}$, and the disc plane. The upper panels refers to the total AM at $R_{\rm v}$ and rotated to the corresponding frame. The bottom panels refers to the AM component along the direction of the disc AM, and rotated accordingly to the disc frame. The color represents the fraction of the AM in the different streams at $R_{\rm v}$.

These figures highlight several non-trivial features. First, they suggest that the three planes are not necessarily aligned with each other, indicating that any correlation among them must be weak. Second, we get the impression that there is a tendency for most of the AM at $R_{\rm v}$ to be carried by one, dominant stream. Third, the three planes seem to be intersecting in one line, which tends to roughly coincide with the dominant stream. These features repeat both for the AM relative to the total AM at $R_{\rm v}$ and for its component along the disc AM. We will quantify these findings and attempt to interpret them below.

5.2   Stream plane versus AM at $R_{\rm v}$

Figure 14 (left) shows the probability distribution function (PDF) of the cosine of the angle between the stream plane and the AM at $R_{\rm v}$, limited to cells in which the inflow velocity is larger than $0.5V_{\rm v}$ (a requirement that makes only a little difference). The PDF shows a *weak tendency for alignment*, with a mean $\langle cos(\theta) \rangle = 0.56$ and median$(cos(\theta)) = 0.60$ compared to 0.5 for a random distribution. The corresponding KS-test rejects the null hypothesis of a random angle with a uniform distribution of cosines at a p level of only 0.001. This alignment being weak provides a hint that most of the AM is carried by one stream, consistent with the examples shown in Fig. 13. A misalignment between the SP and the AM at $R_{\rm v}$ can occur
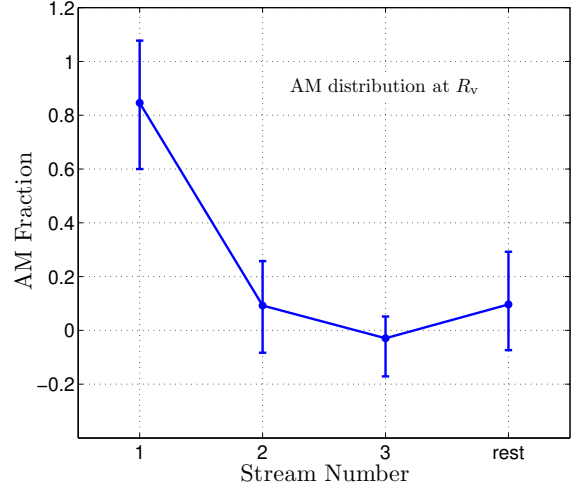

Figure 15. Distribution of AM among the streams at $R_{\rm v}$. Shown are the mean and standard deviation of the relative contribution of the N'th stream to the AM. Only cells with $V_r < -0.5V_{\rm v}$ are considered, and the influx overdensity threshold is 2. On average, one stream carries 84% of the AM!

if the actual best-fit plane to the total influx slightly deviates from the SP as defined here, where it is forced to include the galaxy center. This deviation is natural in the presence of transverse motions in the streams, reflecting the flows from the sheets and voids into the streams. These motions generate non-vanishing impact parameters that represent non-negligible AM, especially for the stream that dominates the AM.

5.3   AM Distribution among the streams

Figure 15 shows the distribution of AM among the streams at $R_{\rm v}$. The streams are ranked by their contribution to the total AM in the shell, and the figure shows the mean and standard deviation of the relative contribution of the N'th stream to the AM. For this figure, the influx overdensity threshold is 2, in order to include a significant fraction of the stream influx, and only inflowing gas with $V_r < -0.5V_{\rm v}$ is considered, in order to focus on the gas that will certainly reach the disc vicinity. The specific choice of these criteria for identifying the streams do not affect the distribution of AM among the streams. We find that in almost all galaxies there is *one dominant stream* that carries on average 84% of the AM. This helps explaining why the AM vector is not necessarily aligned with the stream plane at the same radius. In 70% of the galaxies the stream that dominates the AM is also the stream that carries the largest influx of mass, but in some cases a large impact parameter makes a stream of lower influx carry most of the AM.

5.4   The stream plane versus the disc

Figure 14 (middle) shows the PDF of the cosine of the angle between the stream plane and the disc AM in the whole sample of 336 simulated galaxies. It shows a weak tendency of the disc AM plane to be perpendicular to the streams plane, with $\langle cos(\theta) \rangle = 0.45$ and a median
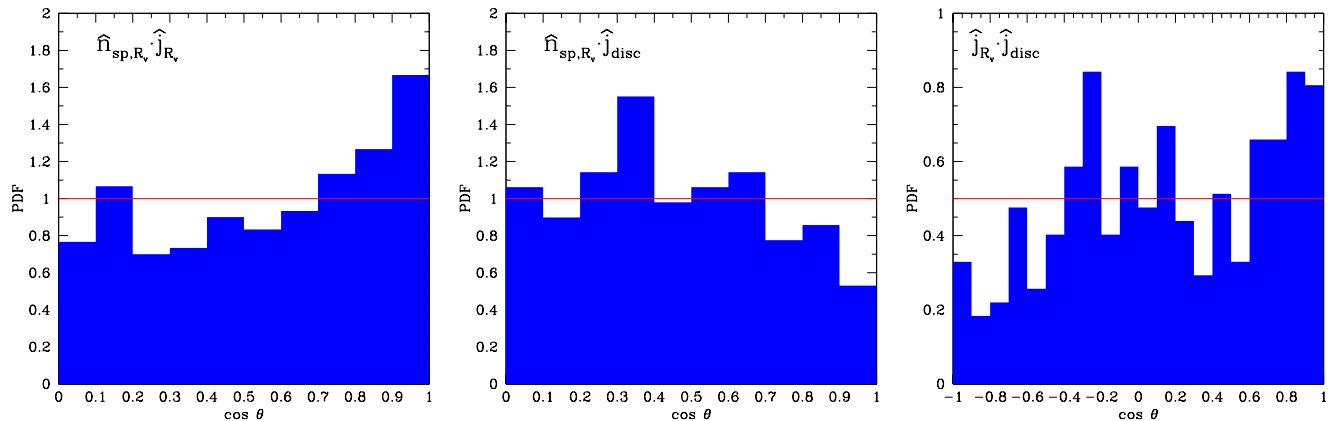
---

[1] The disc AM direction largely coincides with the normal to the disc plane as defined by best fit to the mass distribution.

Figure 14. PDF of the cosine of the angle between pairs of planes. **Left:** The stream plane and the AM at $R_{\rm v}$, with $\langle cos(\theta)\rangle = 0.56$, median= 0.60 and KS $p = 0.001$. **Middle:** the stream plane at $R_{\rm v}$ and the disc AM, with $\langle cos(\theta)\rangle = 0.45$, median= 0.43 and KS $p = 0.03$. **Right:** the AM at $R_{\rm v}$ and the disc AM, with $\langle cos(\theta)\rangle = 0.14$, median= 0.14 and KS $p = 2 \times 10^{-4}$. The AM at $R_{\rm v}$ is restricted to $V_r < -0.5V_{\rm v}$. Note that $\hat{n}$, the normal to the SP, has no preferred orientation, so the associated range of cosine values is $(0, 1)$ rather than $(-1, 1)$.
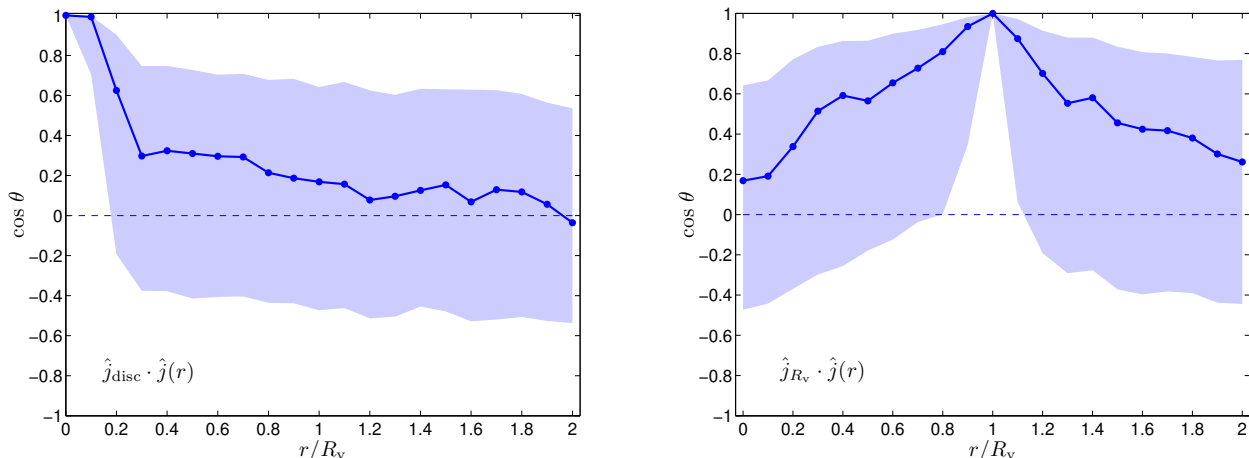

Figure 16. Alignment of AM in shells of different radii. Shown is the median of the cosine of the angle between the AM of the disc (left) or of a shell at $R_{\rm v}$ (right) and the AM in other shells at radius r (and thickness $0.1R_{\rm v}$). The shaded area represents the 1σ scatter about the median for the 336 haloes of the sample. There is a tendency for alignment of AM from outside $R_{\rm v}$ down to $r \sim 0.3R_{\rm v}$, and independently in the immediate disc vicinity $r \leqslant 0.1R_{\rm v}$, but there is an abrupt change of direction at $r = 0.1 - 0.3R_{\rm v}$.

of 0.43 compared to 0.5 for a random angle, and a KS $p = 0.03$. About 60% of the haloes have $cos\theta < 0.5$. A correlation of this nature is consistent with tidal-torque theory, which predicts a tendency for perpendicularity between the AM vector of the galaxy and the intermediate axis of the tidal field, as demonstrated for dark-matter haloes in cosmological N-body simulations (e.g. Porciani et al. 2002a,b; Navarro et al. 2004; Aragón-Calvo et al. 2007). However, our main finding is that this correlation becomes negligibly small for galaxies at the studied highly non-linear stage of evolution. In comparison, there were marginal observational detections of alignments between isolated local disc galaxies and the intermediate axis of the tidal tensor (Dekel 1985; Navarro et al. 2004), as well as failures to detect such an alignment for the massive galaxies at high redshift as studied in hydrodynamical simulations (Hahn et al. 2010).

5.5 AM at $R_{\rm v}$ versus the disc: AM exchange

Figure 14 (right) shows the PDF of the cosine of the angle between the AM at $R_{\rm v}$ ($V_r < -0.5V_{\rm v}$) and the disc AM. The tendency for alignment is stronger than in the other cases, with a KS $p = 2 \times 10^{-4}$ compared to a random distribution, but it is still surprisingly weak, with $\langle cos(\theta)\rangle = 0.14$ and a median of 0.14 compared to zero for the case of no correlation. The excess seen at $cos\theta > 0.6$ and the deficiency below -0.4 each involves only $\sim 10\%$ of the galaxies. One may suspect that the alignment may be weakened by us not considering the time delay between $R_{\rm v}$ crossing and reaching the disc, which is on the order of $500\,{\rm Myr}$. To the extent that the orientation of the AM at $R_{\rm v}$ and the disc plane are not varying drastically over this timescale, we learn that the AM is typically not conserved all the way to the disc.

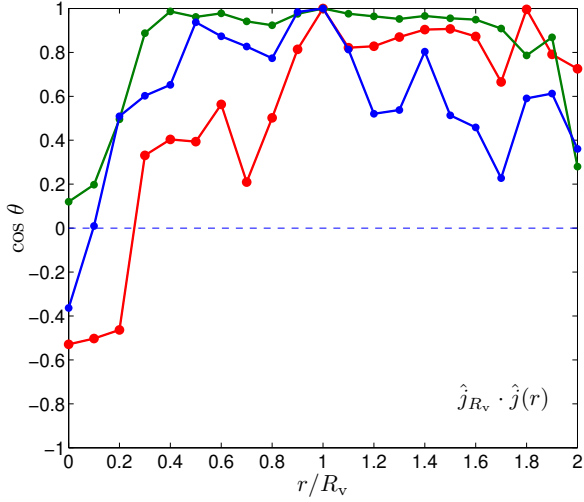Figure 16 addresses the alignment between the AM in

Figure 17. Three realizations from the distribution shown in Figure 16 (right) of the alignment between the AM at R_v and in shells of other radii, displaying different behaviours. The green line (galaxy 250) shows a strong alignment from $r = 1.9R_v$ down to $0.3R_v$, followed by a drop in $\cos(\theta)$ inside this radius toward zero. The red line (66) shows an alignment outside R_v and a change in direction immediately inside R_v leading to a slight anti-alignment inside $0.25R_v$. The blue line (219) is an intermediate case, qualitatively similar to the median shown in Figure 16.
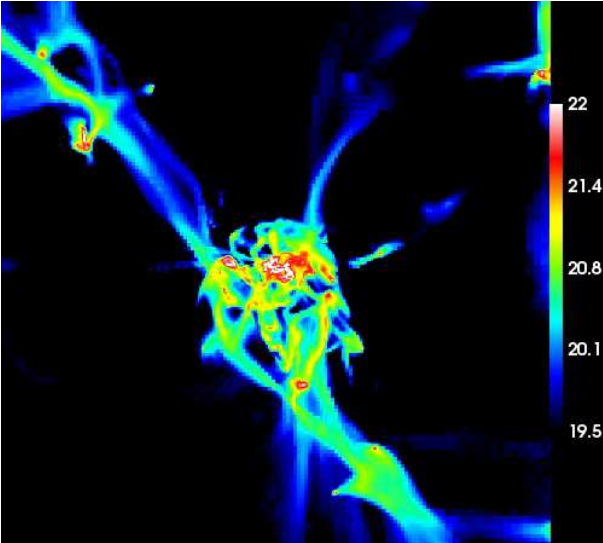

Figure 18. Surface density of cold gas in a galaxy simulated with 70-pc resolution (Ceverino et al. 2010). Beyond the coherent incoming streams coming from more than $100\,\mathrm{kpc}$ away, and the inner disc of radius $\sim 6\,\mathrm{kpc}$ (white), there is a "messy" region of radius $\sim 20\,\mathrm{kpc}$ in which the perturbed distribution of matter results in strong torques and AM exchange — the AM sphere.

shells of different radii, and it describes our most interesting result concerning AM conservation in disk formation. It shows the median of the cosine of the angles, once with respect to the disc AM (left) and once with respect to the shell at R_v. The shells are of thickness $0.1R_v$. We see a tendency for alignment of AM from outside R_v down to $r \sim 0.3R_v$, and in the disc and its immediate vicinity,

$r \leqslant 0.15R_v$, but an abrupt change of AM direction at $r = 0.2 - 0.3R_v$. This marks the inner sphere within which there is a significant exchange of AM, and at the centre of which the actual disc orientation is almost arbitrary compared to the AM at R_v. We term this "the AM sphere".

Figure 17 shows three concrete realizations from the sample that makes the average shown in the right panel of Fig. 16. It shows one case where the AM direction is rather constant from well outside the halo down to the boundary of the AM sphere at $\sim 0.3R_v$, inside which the AM direction significantly deviates from the AM at R_v. It also shows an opposite case where the AM inside most of the virial sphere is far from being aligned with the AM at and outside R_v. The third case is rather typical, similar to the average shown in Fig. 16.

5.6 The AM Interaction Sphere

One should not be totally surprised by the weak alignment between the AM on the halo scale and in the disc vicinity, given what we already have a preliminary notion about how the in-streaming gas joins the disc. Figure 18 shows the surface density of cold gas in a typical galaxy simulated at 70-pc resolution and described in Ceverino et al. (2010). It shows at large radii coherent incoming streams that emerge from outside the virial radius and penetrate toward the inner halo, to eventually end up as an inner disc of radius $\sim 6\,\mathrm{kpc}$. However, the streams break up by collisions, shocks and various instabilities before they reach the disc. Surrounding the disc there is a "messy" region of radius $\sim 20\,\mathrm{kpc}$, which consists of stream fragments and clumps moving in and out in a complex pattern and kinematics. This highly perturbed distribution of matter, including the disc itself, is naturally associated with strong torques and significant AM exchange between the different gas components and possibly between gas, stars and dark matter.

5.7 Intersection of planes and the dominant stream

Back to what we learned from a visual inspection of Fig. 13 regarding the apparent tendency of the three planes to intersect in one line, which is the line defined by the dominant stream in terms of influx of mass and AM. Figure 19 shows the PDFs of cosine of angles between pairs of lines, each corresponding to the intersection of two of the planes or by the dominant stream $\hat{S}_1$.

The strongest alignment is between the dominant stream and the line of intersection between the stream plane and the AM at R_v, namely, $\hat{j}_{R_v} \times \hat{n}_{\mathrm{sp},R_v}$, with a median at $\cos\theta = 0.88$. This is fully consistent with the fact that a single stream indeed carries most of the AM at R_v, and it explains why the stream plane and the AM at R_v are not necessarily aligned with each other.

The dominant stream also tends to be aligned with the lines of intersection between the disc and the two planes at R_v, the stream plane and the AM at R_v, namely, $\hat{j}_{\mathrm{disc}} \times \hat{n}_{\mathrm{sp},R_v}$ and $\hat{j}_{\mathrm{disc}} \times \hat{j}_{R_v}$, but these alignment are weaker, with medians at $\cos\theta = 0.73$ and 0.66 respectively.

Finally, the three planes, despite their very weak alignment with each other, do tend to intersect along one

line, as seen by the PDF of the absolute value of $(\hat{j}_{\rm disc} \times \hat{n}_{\rm sp}) \cdot (\hat{j}_{\rm R_v} \times \hat{n}_{\rm sp})$, for which the median is $\cos\theta = 0.71$.

The emerging picture is that typically *one stream plays the major role in bringing both the mass and the angular momentum into the halo*. This stream determines the AM in the whole inner $0.3R_{\rm v}$ of the halo, the AM sphere. However, the AM in this sphere is only partially reflected in the direction of the disc AM due to *significant AM exchange inside the AM sphere*.

6 DISCUSSION: ON THE ORIGIN OF THE WEB STRUCTURE ABOUT A NODE

Our analysis of the simulations reveal three robust features of the cosmic web in the vicinity of a high-sigma node, namely, the dominance of a single sheet, the dominance of one filament in it, and the preferential contribution from three main filaments embedded in that sheet. In principle, these features should be understood either in terms of the statistics of the initial Gaussian random fluctuation field, or considering the later non-linear evolution involving motions and mergers of structures, or both. This distinction between early and late evolution at a given scale can be replaced by large-scale smoothed linear structure versus small-scale non-linear structure at a given time. While these are open theoretical challenges beyond the scope of the present paper, we mention here preliminary ideas concerning these issues.

As mentioned in §1, based on the Zel'dovich approximation, one can identify the four basic structures of voids, sheets, filaments and haloes with the four possible signatures of the eigenvalues of the local deformation tensor. The spatial extent of each sheet or filament is determined by the coherence length of the relevant eigenvectors. Since a sheet requires a coherence of only one eigenvalue, while a filament requires the simultaneous coherence of two, which is less probable, one can expect the sheets to be in general more extended than the filaments, favoring a configuration of filaments that are embedded in larger sheets, as detected in the simulations. The spatial coherence of the eigenvectors is expected to be especially extended near a node, which can be treated as a high-sigma density peak in the Gaussian random field. The coherence length can in principle be estimated by computing the conditional probability for the value of a given eigenvalue at a distance r from a density peak, in which the density contrast $\delta\rho/\rho \propto (\lambda_1 + \lambda_2 + \lambda_3)$ is given and is high. The average value of the eigenvalue at r is provided by the corresponding conditional two-point correlation function. Most important, the variance about this conditional average is limited by the general variance over space, so the coherence length is expected to be larger about a higher density peak (Dekel 1981; Bardeen et al. 1986). We thus expect long filaments embedded in even more extended sheets to form at an early stage about the massive galaxies that form at the cosmic-web nodes.

The tendency toward a minimum number of filaments and sheets in the vicinity of a node could be understood in terms of the continuity of the eigenvectors of the deformation tensor within the smoothing length $r_{\rm s}$ of the fluctuation field. Within one smoothing length from the node, the eigenvalues at the different points must converge to the vicinity of one set of values. This allows only one dominant filament embedded in one dominant sheet throughout the smoothing volume. For example, two different filaments through a node, with an opening angle of $90°$, say, would require that the eigenvector with the smallest eigenvalue of one filament coincides with one of the eigenvectors with the large eigenvalues of the other filament, which would violate the coherence of the eigenvectors within the smoothing volume. This implies that two filaments with a large opening angle between them far away from the node must merge into a single filament within the $r_{\rm s}$ vicinity of the node (which may correspond in our analysis to two streams inflowing toward the node in opposite directions along the same line). The continuity implies that the filaments merge smoothly in a bifurcation point at a distance $\sim r_{\rm s}$ from the node, such that they form a swallow-tail structure, like a splitting fork in a road, similar to what is predicted in Fig. 10 of Arnold et al. (1982) and hinted in Fig. 2 above. Analogous considerations apply to the presence of one dominant sheet. The relevant smoothing scale in our study is the halo virial radius about the node, which stretches to a Lagrangian region of a few virial radii (a mean density contrast of 180 within $R_{\rm v}$ translates to a comoving radius of $5.6R_{\rm v}$). We therefore expect the sheet about a node to extend to a few virial radii, as detected in the simulations.

A somewhat different quantitative approach to the properties of the cosmic web is based on the "skeleton" of critical lines (filaments) connecting critical points (nodes), mastered by Novikov et al. (2006), Pogosyan et al. (2009) and Pichon et al. (2010). It makes use of the Hessian H, the tensor consisting of the second spatial partial derivatives of the density field, whose local eigenvalues are denoted $h_1 \geqslant h_2 \geqslant h_3$. The primary skeleton is defined as the set of points where $h_1 + h_2 \leqslant 0$ and where the gradient of the density field is an eigenvector of the Hessian, and corresponds to the largest eigenvalue, $H \cdot \nabla\rho = h_1\nabla\rho$. In this formalism, the filaments connect the density maxima at the nodes and the saddle points mid-way between maxima. The eigenvector corresponding to h_1 defines the preferred direction for the dominant filament within the $r_{\rm s}$ vicinity of the maximum. Outside $r_{\rm s}$, one expects the single filament to bifurcate into two where $h_1 = h_2$, i.e., where the two directions are locally equivalent. This creates three filaments in a plane, as detected. The sequence of bifurcations as one receded from the node indicates a shift from two filaments along a single line inside the virial radius, to three filaments in a plane near and outside the virial radius, and to a larger number of filaments in more sheets further away from the nodes, until these filaments construct the three-dimensional web on scales much larger than $r_{\rm s}$.

Being fed by three dominant filaments at the virial scale is not an obvious property of the nodes in a general three-dimensional network. For example, in a symmetric cubic lattice each node is fed by six filaments along three lines. On the other hand, with only two filaments per node, one cannot construct a three-dimensional web, not even a two-dimensional network, so three is the minimum average number of filaments per node. Once we found that the filaments near a node tend to be confined to one plane, and obtained hints concerning the possible origin of this dominant plane, the question reduces to the appearance of three filaments in the effective
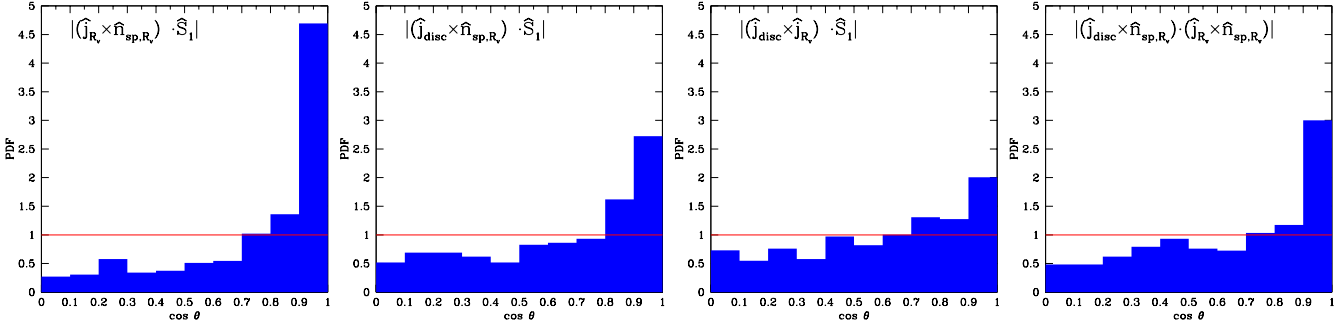
Figure 19. Alignment between the intersection of planes and the dominant stream: the AM at R_v ($\hat{j}_{R_v}$), the normal to the stream plane ($\hat{n}_{sp}$), the disc AM ($\hat{j}_{disc}$), and the vector along the dominant stream at R_v ($\hat{S}_1$). The means are: 0.76, 0.65, 0.60, 0.71. The medians are: 0.88, 0.73, 0.66, 0.71. The KS p values are smaller than unity by many orders of magnitude in all cases.

two-dimensional space about the node. This issue has been addressed in the early mathematical analysis of caustics that bound filaments and sheets following the quasi-linear description of structure development a la Zel'dovich. Arnold et al. (1982); Shandarin & Zeldovich (1989) showed in this analysis that a node of three filaments is the natural configuration in two-dimensional space. They also argue that the swallow-tail configuration of these three filaments is common. This theory of caustics is yet to be properly related to the structure in a three-dimensional Gaussian random field.

In two dimensions, a symmetric configuration with three filaments per node is the hexagonal grid, or the honeycomb, as opposed to the cubic grid with four filaments per node. The empty spaces in a honeycomb encompass bigger spherical voids than in a cubic grid, and since the underdense voids are dynamically driven to become spherical by the gravitational forces, this dynamical effect may drive the cosmic web into a honeycomb configuration. Another possibly relevant property of the hexagonal grid, known as the honeycomb theorem (Hales 2001), says that the total length of filaments in a honeycomb is the minimum possible length among all the partitions of the plane into regions of equal area. However, the direct relevance of this to the cosmic web is yet to be addressed.

7 CONCLUSION

Our results shed new light on how massive galaxies at high redshift acquire their mass and angular momentum. It has been known for a while, based on cosmological simulations, that the baryons flow in along narrow streams that follow the dark-matter filaments of the cosmic web toward the high-density peaks at the nodes where they intersect (Birnboim & Dekel 2003; Keres et al. 2005; Dekel & Birnboim 2006; Ocvirk et al. 2008; Dekel et al. 2009). These streams consist of cold gas and a spectrum of merging galaxies. We now find that at the few virial radii vicinity of the galaxy, the streams tend to be confined to a stream plane, and embedded in a flat pancake that carries $\sim 20\%$ of the influx. There are on average three significant streams, of which one typically carries more than half the mass inflow.

This structure of filaments that are embedded in an

extended sheet is unique to the neighborhood of massive galaxies at high redshift, where they reside in the high-sigma density peaks that are associated with the nodes of the cosmic web. On larger scales, the filaments are the intersections of coherent sheets that are tilted relative to each other and together encompass big voids. The transition from a three-dimensional web to a planar distribution of streams on the virial scales near the nodes introduces a non-trivial theoretical challenge. So is the tendency to have three major streams, of which one dominates. We mention very crude hints for the origin of these phenomena in section §6.

Small transverse velocities of the streams at large distances induce non-zero impact parameters of the streams relative to the galaxy centre, and the associated angular momentum is transported with the streams into the galaxy (see also Pichon et al. 2011; Kimm et al. 2011). The fact that at later times the gas originates from larger distances indicates that it carries larger specific AM, which gives rise to disk growth inside out. The major stream typically carries $\sim 80\%$ of the AM near R_v. This dominant stream and the galaxy centre define the AM plane in the outer halo and outside it, which does not necessarily coincide with the stream plane. The AM direction is preserved as the stream penetrates the outer halo and till it reaches $r \sim 0.3R_v$. Inside the sphere of $0.3R_v$, the coherent streams shock, break and interact with the disc, so the mass distribution and kinematics become asymmetric and complex. This leads to significant AM exchange between the different components due to strong torques. The disc orientation at the centre of this AM sphere turns out to be quite arbitrary.

Much of the analytic and semi-analytic modeling of disc formation is based on the very useful simplifying assumption that the gas conserves its AM as it flows in through the halo, implying that the disk radius scales with the virial radius times a constant spin parameter ~ 0.05 (Fall & Efstathiou 1980; Bullock et al. 2001; Mo et al. 1998). Our results here indicate that this assumption is invalid as far as the direction of the disc AM is concerned. However, the jury is still out on the extent to which the amplitude of the disc AM approximates the AM of the inflowing mass, and its implications on the disc size and inner structure. This is work in progress. We note that the significant misalignment may be associated with a change of only a factor of two in the spin amplitude. This is similar to the results concerning the validity of the tidal-torque theory

in predicting the direction and amplitude of the halo spin (Porciani et al. 2002a).

Our evaluation of the limited artificial tendency of the discs to align with the simulation grid (§C) indicates that our conclusions are not biased by this numerical effect. A much stronger artificial effect is required in order to hide a strong alignment between the disc and the AM at R_v. Indeed, similar studies using zoom-in cosmological simulations with a resolution more than ten times better reveal similar results (Hahn et al. 2011).

The direct relevance of the results obtained here for massive discs at high redshift to low-redshift discs should be considered with caution, as the latter probably develop under slow, wide-angle accretion rather then by the intense, narrow, high-redshift streams (Dekel & Birnboim 2006). We expect many of the massive discs analyzed here at $z = 2.5$ to evolve into early-type galaxies at low redshift (Dekel et al. 2009; Ceverino et al. 2010), while today's discs arise from smaller progenitors, typically with quiet merger histories after $z \sim 1$ (Martig et al. 2012), and in which feedback slows down star formation and allows the late formation and maintenance of thin discs (Governato et al. 2010; Guedes et al. 2011).

REFERENCES

Adelman-McCarthy J. K., 2008, ApJS, 175, 297
Aragón-Calvo M. A., Jones B. J. T., van de Weygaert R., van der Hulst J. M., 2007, A&A, 474, 315
Aragón-Calvo M. A., Platen E., van de Weygaert R., Szalay A. S., 2010, ApJ, 723, 364
Aragón-Calvo M. A., van de Weygaert R., Jones B. J. T., 2010, MNRAS, 408, 2163
Aragón-Calvo M. A., van de Weygaert R., Jones B. J. T., van der Hulst J. M., 2007, ApJ, 655, L5
Arnold V. I., Shandarin S. F., Zeldovich Y. B., 1982, Geophysical and Astrophysical Fluid Dynamics, 20, 111
Aubert D., Pichone C., Colombi S., 2004, MNRAS, 352, 376
Bardeen M. J., Bond R. J., Kaiser N., Szalay S. A., 1986, ApJ, 304, 15
Birnboim Y., Dekel A., 2003, MNRAS, 345, 349
Bond J. R., Kofman L., Pogosyan D., 1996, Nature, 380, 603
Bournaud F., Dekel A., Teyssier R., Cacciato M., Dadd E., Juneau S., Shankar F., 2011, arXiv:1107.1483v2
Bullock J. S., Dekel A., Kolatt T. S., Kravtsov A. V., Klypin A. A., Porciani C., Primack J. R., 2001, ApJ, 555, 240
Cacciato M., Dekel A., Genel S., 2011, arXiv:1110.2412
Ceverino D., Dekel A., Bournaud F., 2010, MNRAS, 404, 2151
Ceverino D., Dekel A., Mandelker N., Bournaud F., Burkert A., Genzel R., Primack J., 2011, arXiv:1106.5587
Colberg J. M., Krughoff K. S., Connolly A. J., 2005, MNRAS, 359, 272
Colless M., 1999, Phil. Trans. R. Soc. Lond. A, 357, 105
Davis M., Efstathiou G., Frenk C. S., White S. D. M., 1985, ApJ, 292, 371
Dekel A., 1981, A&A, 101, 79
Dekel A., 1985, ApJ, 298, 461
Dekel A., Birnboim Y., 2006, MNRAS, 368, 2
Dekel A., Birnboim Y., Engel G., Freundlich J., Goerdt T., Mumcuoglu M., Neistein E., Pichon C., Teyssier R., Zinger E., 2009, Nature, 457, 451
Dekel A., Sari R., Ceverino D., 2009, ApJ, 703, 785
Dekel A., West M. J., 1985, ApJ, 288, 411
Doroshkevich A. G., 1970, Astrophysics, 6, 320
Dubois Y., Teyssier R., 2008, A&A, 477, 79
Fall M. S., Efstathiou G., 1980, MNRAS, 193, 189
Fumagalli M., Prochaska X., Kasen D., Dekel A., Ceverino D., Primack J. R., 2011, arXiv:1103.2130v2
Gay C., Pichon C., Le Borgne D., Teyssier R., Sousbie T., Devriendt J., 2010, MNRAS, 404, 1801
Genel S., Naab T., Genzel R., Förster Schreiber N. M., Sternberg A., Oser L., Johansson P. H., Davé R., Oppenheimer B. D., Burkert A., 2012, ApJ, 745, 11
Genzel R., Bukert A., Bouche N., 2008, ApJ, 687, 59
Genzel R., Tacconi L. J., Eisenhauer F., Frster Schreiber N. M., Cimatti A., Daddi E., Bouche N., Davies R., Lehnert M. D., Lutz D., Nesvadba 2006, Nature, 442, 786
Goerdt T., Dekel A., Sternberg A., Gnat O., Ceverino D., 2011, arXiv:1109.0000
Governato F., Brook C., Mayer L., Brooks A., Rhee G., Wadsley J., Jonsson P., Willman B., Stinson G., Quinn T., Madau P., 2010, Nature, 463, 203
Guedes J., Callegari S., Madau P., Mayer L., 2011, ApJ, 742, 76
Hahn O., Carollo C. M., Porciani C., Dekel A., 2007, MNRAS, 381, 41
Hahn O., Dekel A., Ceverino D., Danovich M., Abel T., 2011, arXiv:1111.0000
Hahn O., Porciani C., Dekel A., Carollo C. M., 2009, MNRAS, 398, 1742
Hahn O., Porciani C., Marcella Carollo C., Dekel A., 2007, MNRAS, 375, 489
Hahn O., Teyssieri R., Marcella Carollo C., 2010, MNRAS, 405, 274
Hales T. C., 2001, DISCR.COMPUT.GEOM., 25, 1
Hopkins P. F., Keres D., Murray N., Quataert E., Hernquist L., 2012, arXiv:1111.6591
Hucra J., Latham D., Tonry J., 1983, ApJS, 52, 89
Keres D., Katz N., Weinberg D. H., Dave R., 2005, MNRAS, 363, 2
Kimm T., Devriendt J., Slyz A., Pichon C., Kassin S. A., Dubois Y., 2011, arXiv:1106.0538
Klypin A., Trujillo-Gomez S., Primack J., 2011, arXiv:1002.3660v4
Klypin A. A., Shandarin F. S., 1983, MNRAS, 204, 891
Martig M., Bournaud F., Croton D., Dekel A., Teyssier R., 2012, arXiv:1201.0000
Mo H. J., Mao S., White S. D. M., 1998, MNRAS, 295, 319

Navarro J. F., Abadi M. G., Steinmetz M., 2004, ApJ, 613, L41

Noh Y., Cohn D. J., 2011, MNRAS, 413, 301

Novikov D., Colombi S., Doré O., 2006, MNRAS, 366, 1201

Ocvirk P., Pichon C., Teyssier R., 2008, MNRAS, 390, 1326

Oser L., Ostriker J. P., Naab T., Johansson P. H., Burkert A., 2010, ApJ, 725, 2312

Pichon C., Gay C., Pogosyan D., Prunet S., Sousbie T., Colombi S., Slyz A., Devriendt J., 2010, AIPC, 1241, 1108

Pichon C., Pogosyan D., Kimm T., Devriendt Y., Dubois Y., 2011, arXiv:1105.0210v1

Pogosyan D., Bond J. R., Kofman L., 1998, J. R. Astron. Soc. Can., 92, 313

Pogosyan D., Pichon C., Gay C., Prunet S., Cardoso J. F., Sousbie T., Colombi S., 2009, MNRAS, 396, 635

Porciani C., Dekel A., Hoffman Y., 2002a, MNRAS, 332, 325

Porciani C., Dekel A., Hoffman Y., 2002b, MNRAS, 332, 339

Shandarin S. F., Zeldovich Y. B., 1989, Reviews of Modern Physics, 61, 185

Shen J., Abel T., Sheth R. K., 2006, ApJ, 645, 783

Sousbie T., 2011, MNRAS, 414, 350

Sousbie T., Pichon C., Kawahara H., 2011, MNRAS, 414, 384

Springel V., White S. D. M., Jenkins A., Frenk C. S., 1996, Nature, 435, 603

Tacconi L. J., 2008, ApJ, 680, 246

Teyssier R., 2002, A&A, 385, 337

Vazza F., Brunetti G., Gheller C., Brunino R.and Brüggen M., 2011, A&A, 529, 17

White S. D. M., 1984, ApJ, 286, 38

Zeldovich Y. B., 1970, A&A, 5, 84

This paper has been typeset from a TeX/ LaTeX file prepared by the author.

APPENDIX A: THE MARE NOSTRUM SIMULATION

The Horizon Mare Nostrum cosmological simulation follows the evolution of a cubic box of side $50\,h^{-1}\mathrm{Mpc}$ (comoving), containing 1024^3 dark matter particles of $1.17 \times 10^7 \mathrm{M}_\odot$ each and 4×10^9 gas cells. It uses the Eulerian AMR code RAMSES (Teyssier 2002), which is based on a graded octree structure with a cell by cell refinement. Each cell is refined if the dark matter mass exceed 8 times the dark matter particle mass or if the gas mass exceeds 8 times the initial gas mass resolution. Shocks and contact discontinuities are not refined. The former has been shown (Teyssier 2002) not to lead to spurious effects in the cosmological context. The latter could lead to an underestimate the subsonic turbulence induced by gravitational collapse, but it has been estimated to stay below 10-15% of the total thermal or gravitational energy (Vazza et al. 2011, and references therein). The refinement criteria are based on gradients of the flow variables in a given cell. The N-body solver uses a Particle-Mesh scheme and the Poisson equation is solved using a multigrid solver. The hydrodynamical solver uses an unsplit second order Godunov method.

The cosmological model used is the ΛCDM model with $\Omega_\Lambda =$
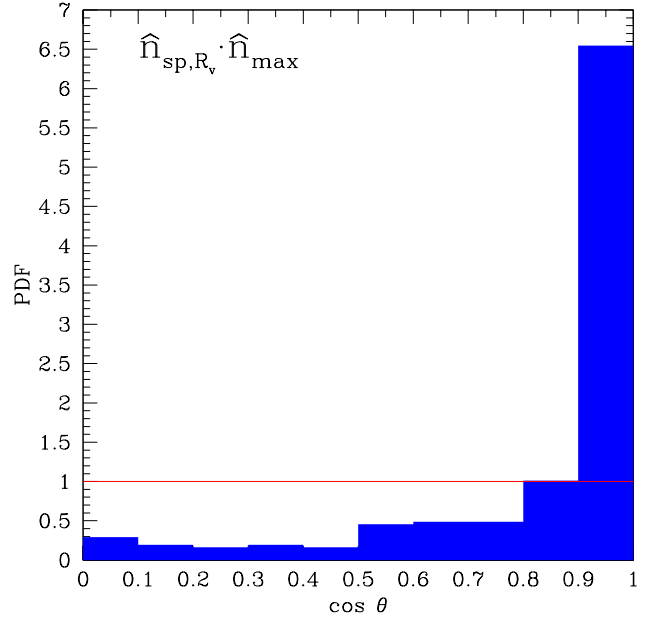

Figure 20. PDF of the cosine of the angle between the stream plane as defined in §3.1 and the maximum-influx plane. We see a strong alignment, with a median of $\cos\theta = 0.96$.

0.7, $\Omega_\mathrm{m} = 0.3$, $\Omega_\mathrm{b} = 0.045$, $h = 0.7$ and $\sigma_8 = 0.95$. Dark matter haloes are identified using the AdaptaHop algorithm. The physical processes for galaxy formation implemented in the RAMSES code include radiative cooling, UV background radiation, star formation and SN feedback. Gas can cool radiatively to a minimum temperature of $10^4 K$ with a rate depending on the local metallicity. Star formation is included for gas above a threshold density $n_H > n_0$, with $n_0 = 0.1\,\mathrm{cm}^{-3}$, designed to match the Kennicutt SFR law with an efficiency of 5% per free-fall time. UV heating is included using the Haardt and Madau background model. SN feedback and the associated metal enrichment are implemented based on the blast-wave model described in (Dubois & Teyssier 2008), where 50% of the SN energy is deposited as bulk motion in a gas bubble of a certain radius, and the other half is assumed to be radiated away. High-density regions are described by a polytropic equation of state with $\gamma = 5/3$ to model the complex, multi-phase structure of the ISM.

APPENDIX B: MAXIMUM INFLUX PLANE

In §3.1 we described our main algorithm for defining the stream plane at a given spherical shell as the best fit great circle to the angular positions of the three dominant streams. An alternative way to defining the plane is by maximizing the influx through a belt about the great circle (e.g., Aubert et al. 2004). This includes the influx in all streams as well as the pancakes. In a concrete example, we use a width of $\pm\pi/9$ for this ring, such that it covers about one third of the spherical shell. This algorithm has been applied to the whole sample of haloes, in a spherical shell of thickness $0.1R_\mathrm{v}$ about $r = R_\mathrm{v}$.

Figure 20 shows the distribution of the cosine of the angle between this maximum-influx plane and the stream plane as defined in our main analysis, §3.1. We find that in the vast majority of the haloes the stream planes defined by the two methods practically
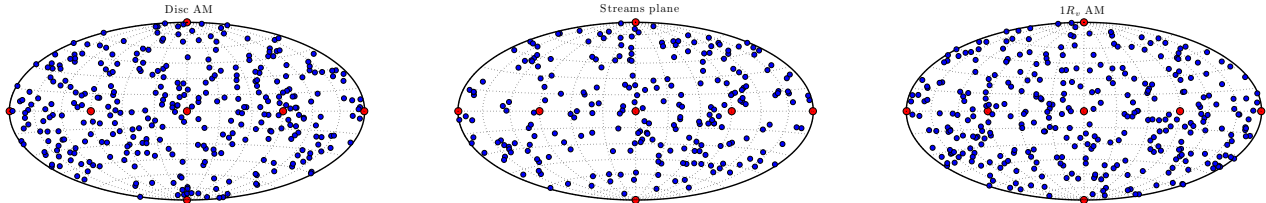
Figure 21. Numerical alignment. Hammer-Aitoff projection showing for each galaxy the direction of the normal to the plane in question (blue dots). The red dots represent the 6 directions of the simulation grid axes. **Left:** disc plane. **Middle:** stream plane at $R_{\rm v}$. **Right:** angular momentum at $R_{\rm v}$. No obvious clustering of the blue dots about the red dots is noticeable, indicating that the numerical alignment with the simulation grid is weak.
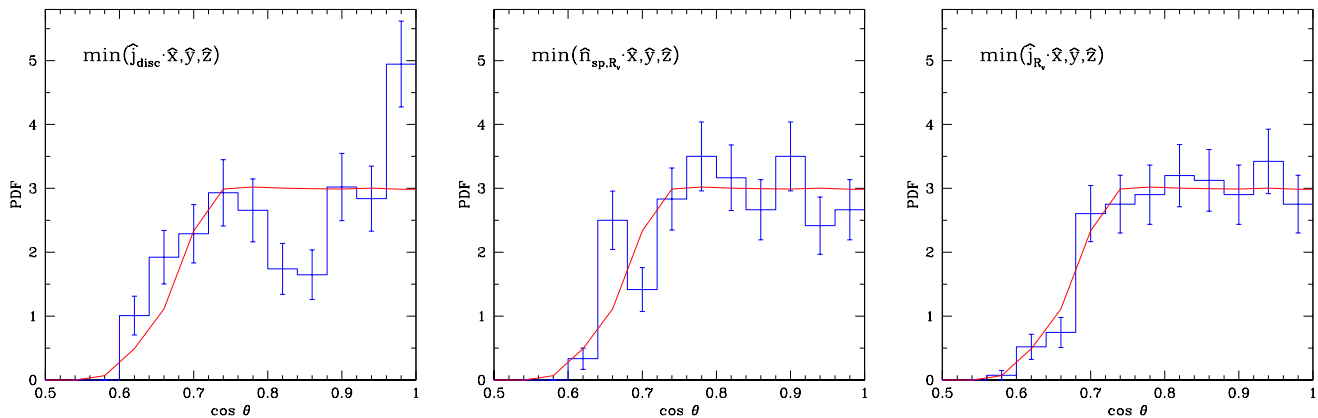

Figure 22. Numerical alignment. The distribution of the cosine of the angle between the normal to the plane in question and the closest simulation grid axis (blue). It is compared to the corresponding distribution for random plane orientations (red). **Left:** disc plane. **Middle:** stream plane at $R_{\rm v}$. **Right:** angular momentum at $R_{\rm v}$. The disc shows a weak numerical alignment signal involving $\sim 20\%$ of the discs at the level of $\Delta \cos \theta \sim 0.08$.

coincide, with a median of $\cos \theta = 0.96$ for the angle between the two planes. This is an encouraging evidence for the robustness of our analysis.

APPENDIX C: SIMULATION AXES BIAS

A potential caveat in our analysis of preferred planes is the numerical tendency for artificial alignment of these planes with the simulation grid. A multigrid Poisson solver, and in particular the hydrodynamical solver, create non-physical forces along the preferred Cartesian directions of the simulation grid, which act to align the mass distribution with the grid (Hahn et al. 2010). This is especially relevant for the galactic disc plane, which involves scales not much larger than the resolution scale, but it may also propagate to the sheets on larger scales. This artificial alignment is expected to be stronger at lower redshifts, where the discs might have had enough time to relax to the closest grid direction, so we expect our analysis of massive galaxies at $z = 2.5$ to be less vulnerable to this numerical effect, despite the 1-kpc resolution.

In Fig. 21, for each of three planes in question, we display the distribution of directions of the normals to this plane (a blue dot per galaxy). The planes are the disc plane, the stream plane and the angular momentum at $R_{\rm v}$. The positions of the six simulation grid axes are marked (red dots). A tendency for numerical alignment

would appear as clustering of the blue points about the red points. For the three planes in question, the distribution of blue points appears to be isotropic. This suggests that the numerical alignment is weak, even for the disc plane.

In Fig. 22 we show the PDF of the cosine of the minimum angle between the normal to the plane in question and the any of the simulation grid axes. The count in each bin of $\cos \theta$ is associated with a Poisson error bar. This distribution is compared to a null hypothesis of isotropic distribution of plane normals. For the disc plane, a KS-test marginally rejects the null hypothesis with a p-value of 0.02. Inspecting the PDF, we see a significant deficiency of counts in the range $\cos \theta = 0.80 - 0.88$ involving $\sim 10\%$ of the galaxies, and an excess involving a similar fraction of the galaxies at $\cos \theta = 0.96 - 1.00$. We interpret this as an offset of $\Delta \cos \theta \sim 0.08$ involving $\sim 20\%$ of the galaxies. The overall shift of the median $\cos \theta$ compared to the random distribution of plane normals is about 0.01. This small effect represents the level of error that we should assign to any measure of alignment between the disc and other planes. The stream plane and the angular momentum at $R_{\rm v}$ do not show a noticeable numerical alignment with the simulation grid. The KS-test p-values are 0.83 and 0.5 respectively, and the shifts in the median $\cos \theta$ are less than 0.01.
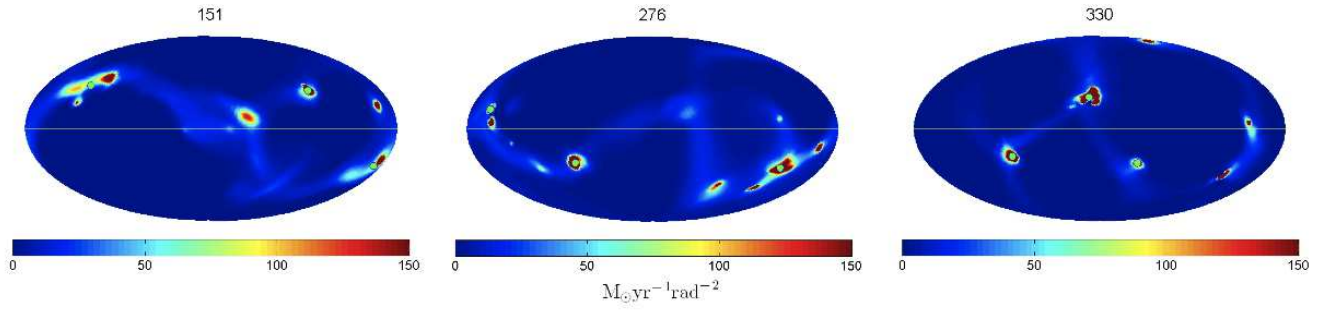
Figure 23. Poor stream planes. Hammer-Aitoff projection for 3 haloes, similar to Figure 3, showing the three worst cases for a stream plane.

APPENDIX D: POOR STREAM PLANES

Figure 23 shows the 3 worst cases for a stream plane. The streams in the middle and right panels do not lie on one plane that includes the halo centre. On the other hand, the halo shown in the left panel has three main streams that do define a plane and are embedded in a visible pancake, but it also shows two other streams that do not lie on the same plane.